Optical Non-Destructive Surface Inspection and Automatic Classification of Cast Iron Automotive Part

by

Raunak Borwankar

A Dissertation

Submitted to the Faculty

of the

WORCESTER POLYTECHNIC INSTITUTE

in partial fulfillment of the requirements for the

Master of Science

in

Electrical and Computer Engineering

April 2017

APPROVED BY:

Dr. Reinhold Ludwig
ECE Department, WPI, Advisor

Dr. Xinming Huang
ECE Department, WPI, Committee member

Dr. Yehia Massoud
ECE Department, WPI, Committee member
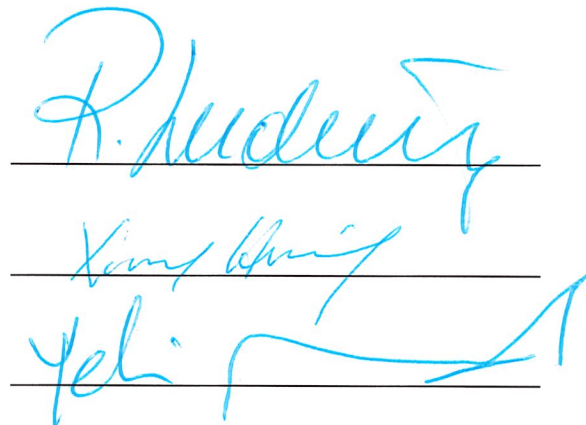
Abstract

Over the past decade, research into computer vision has proliferated with the goal to incorporate artificial intelligence into a wide range of applications. These applications can be as sophisticated as intelligent assistants in smartphones and self-driving cars or as mundane as text and face recognition. While most of these applications are software based, they represent unique challenges when it comes to industrial implementation.

This thesis concentrates on an optical non-destructive testing (NDT) and automatic classification methodology using customized image processing techniques. In contrast to conventional spatial analyses, which are highly susceptible to noise and human perception, our proposed transform domain approach provides a high degree of robustness and flexibility in feature selection and hence a better classification efficiency. Our presented algorithm classifies the Part-Under-Test (PUT) into two bins of either acceptable or faulty using transform domain techniques in conjunction with a classifier. Because the classification is critically dependent on the features extracted from these images, a sophisticated scalable database was created.

This thesis applies transform domain techniques such as Discrete Wavelet Transform (DWT) and Rotated Wavelet Transform (RWT) for feature extraction and then classifies the PUT based on those features. Although, this approach achieves promising classification efficiency, it does not meet industrial standards. It was concluded that in order to achieve those standards, the effect of emissivity fluctuations of the PUT should be negated. The research was then extended to apply an image acquisition algorithm in the form of shape from polarization. The approach exploits the partially linearly polarization of reflected light from the PUT surface. It was observed that this method could not only detect if the PUT is faulty or fault free, but also highlight the locations of the flaws.

Acknowledgment

Most importantly, I would like to extend my sincere gratefulness to Dr. Reinhold Ludwig for being such an encouraging thesis advisor. He has always supported me and provided me with great advice. Through his actions, he motivated me to trust my instincts. I am fortunate to have an advisor of such immense knowledge and patience.

I would like to express my sincere gratitude to Dr. Xinming Huang and Dr. Yehia Massoud for taking time out of their busy schedule to serve on my M.S. Thesis Committee. I am honored to have such a reputable committee.

I thank Dr. Gene Bogdonav for his valuable inputs and extraordinary feedback which has helped shape this work significantly.

I express thanks to my parents, Mukund Borwankar and Rashmi Borwankar and my sister Swara Joshi who have been cheering me and stood by me through the good and bad times. Finally, I thank my friend Akshata Karekar who has always aspired me to believe in myself.

I would also like to thank my fellow colleagues Kuldeep Gill and Devdip Sen for their valuable thoughts and contributions. Best of luck to you all!

Table of Contents

List of Figures

List of Tables

Chapter 1 Introduction

Because of dramatic increases in recent consumer product recalls, the rapid, nondestructive inspection of high-volume metallic components has become the center of attention in many industries, particularly the automotive sector. Various companies have relied on human perception or interpretation to ultimately decide on the quality of the components under test. Unfortunately, visual inspection of complex-shaped parts requires extreme concentration and consistency. When it comes to consistency, no human can match the level of regularity achieved by computer vision systems. Over the past decade, there has been significant growth in computer vision and artificial intelligence. As a result, extensive research is taking place in these areas and the practical applications range from image retrieval to image comparison, from face or speech recognition to age classification. However, the cost-effective, automatic inspection of high-volume components has remained an active research area.

1.1 Review of Existing Solutions

In this section, we will discuss some of the existing nondestructive testing (NDT) techniques implemented in the manufacturing industry. One of the most common NDT techniques implemented in industry is acoustic resonance [7]. Beyond acoustic resonance, we will briefly discuss magnetic particle testing, eddy current testing, laser testing, and optical testing. Nondestructive testing techniques for the diagnosis of defects in solid materials can follow three steps, i.e., detection, localization, and characterization. Acoustic Resonance Testing (ART) is a non-destructive test that uses the vibrational characteristics of an object to find potentially dangerous defects. Acoustic resonance testing is a rapidly growing NDT method used for 100% testing of a wide range of products. References [7, 8] propose a method that is

designed for rapid detection of cracks and other manufacturing-related flaws, with time per part typically being less than a second. ART is a whole-part test, implying that measurements taken at one place can indicate defects anywhere. ART can be completely automated and make objective, quantitative judgments, thereby eliminating human error. ART uses the fact that a part's physical structure causes it to have a distinct and unique set of characteristic, harmonic frequencies. When a part is impacted by an external force, or dropped onto a suitable surface it resonates at frequencies specific and unique to each part, which are the natural modes. These modes are affected by cracks and other internal material related defects causing a change in the resonant frequencies. Every part with the same physical properties will have the same vibration properties, and any flaw will cause this vibration to change. After a hammer impact, the characteristic frequencies of the part will be excited and every other frequency will quickly attenuate. This resonance can be captured using a simple microphone to obtain the resonance spectrum and by measuring the location and amplitude of several peaks of the part's dynamic response and comparing these values to a database of acceptable values, parts with defects can be quickly separated. ART can be used to find parts with out-of-tolerance dimensions, voids, and cracks, among other things. While the test will not determine the cause of rejection, with appropriate transducer sensitivity and software it can reliably find faults anywhere in a part. ART is also being used on some automotive production lines to ensure 100% compliance with specifications. It is well-suited for quality assurance on automotive parts, piping sections, power transformer, and other applications where fast and dependable flaw detection is critical. We will discuss some of these applications below.

Reference [1] proposes a nondestructive, acoustic emission method of detecting cracks caused by an automotive stamping process. Continuous monitoring of crack detection is required

for a high quality and reliable automotive manufacturing process that are based on nondestructive tests. In addition, it is necessary to employ an optimized method that adapts itself to the surrounding environment and to a facility's characteristics. In their approach, they propose a comparative method using amplitude distribution between cracked and un-cracked components. As the cracked components from the automotive stamping process release low elastic energy, a filter is employed that was set at a specific frequency band. An amplitude distribution method was applied along with ratio conversion to achieve a digitization. In other experiment of monitoring the spot weld quality, [2] proposes a portable, online, real-time, through-transmission, continuous wave ultrasonic non-destructive evaluation system. They employed ultrasonic transducers attached to the top and bottom electrode arms of the spot welding machine. They show an improvement in results compared to destructive tests.

Partial Discharge (PD) detection based on ART technique is gaining importance due to the advantages like being nondestructive, on-line, having the possibility of location of PD sources, etc. Acoustic resonance in oil filled transformers and reactors is associated with degradation of the core and tank assemblies as well as the insulation system. Detection and analysis of such resonance leads to early detection of flaws in these power equipment's. Reference [3] identifies the characteristics of acoustic resonance signals from utility inductive reactors for developing a monitoring system for such equipment. Acoustic resonance measurements were carried out on a number of reactors, and the results obtained were analyzed and compared with concurrent dissolved gas in oil analysis. The use of the results for developing a monitoring system is discussed, for example, reference [4] experimented with testing of power transformers. In addition to PD signals, ART data acquired may contain acoustic resonance signals from different sources like electrical, thermal, mechanical, environmental, etc. For a

3

realistic analysis of such ART data, it is essential to eliminate unwanted signals (noise). Different defects generate acoustic resonance signals with different characteristics, which help in discrimination of PD from noise. This requires precise knowledge of the characteristics of individual sources. Simulation of known types of defects in power transformers has helped to study their ART characteristics and differentiate PD sources from noise source.

Next, we turn our attention to other area where acoustic resonance is successfully used to conduct NDT. Reference [5] uses higher order statistics (HOS) to characterize acoustic resonance events in ring-type samples like steel pipes. Firstly, the diagonal bi-spectrum allows the separation of the primary (original) deformation from the reflections produced mainly in the suppressed chord. Second, a cumulate-based independent component analysis may be used before the bi-spectrum, as a preprocessing complement, in the case of multiple-source and multiple-channel recordings. This algorithm suppresses the mutual influence of the sources and sensors. Acoustic resonance technique incorporated with the hydrostatic testing has been successfully developed for high-pressure stainless steel pipe evaluation by [6]. This technique employed 100 kHz and 300 kHz frequencies of the acoustic resonance sensors that were mounted on the pipe material. Various hydrostatic pressures starting from zero to 120 bars were applied to the pipe and ART signals from both sensors were captured by a personal computer via data acquisition card. The Crest factor and AR energy, which are the processed AR parameters, were used to indicate crack initiation or growth in the pipe material during pressurized. The test results show several micro cracks have been found in the both defected pipes by microstructure test. Along similar lines, reference [9] proposes a real time crack detection system in order to be used as a quality control strategy for synthesized metallic pieces. The signal-processing algorithm is based on the spectral analysis of the signal measured by means of acoustic

4

resonance inspection. The spectrum is obtained by applying an FFT based chirp algorithm and from the resonance frequencies a minimum Euclidean distance algorithm, controlled by the false alarm probability, is applied to parts that are cracked or defective pieces from the production system. The system has been tested in different production environments and with different types of pieces giving for all cases satisfactory results. Therefore, the advantage of using AR technique is that it provides sufficient sensitivity to detect a micro cracking propagation in pipe material.

We next discuss another NDT technique in the form Magnetic particle Testing (MT) that uses ferromagnetic materials after being magnetized. The existence of a discontinuity generates a leakage magnetic field. This magnetic field is formed when lines of magnetic induction leave and enter the surface. It can absorb magnetic particle on work piece surface and form visible indications in the right light, thereby revealing the location, shape, size and severity of the discontinuity. Therefore, magnetic particle indications can be used to reveal defects in ferromagnetic material and its products. Magnetic particle testing can detect the exposed small defects, which cannot be directly observed by the naked eye, or by a magnifying glass, and can detect near-surface defects, which are not exposed but are few millimeters below the surface [10]. Although this method can also be used to detect volume type defects such as gas pole, slag and incomplete fusion, it is more sensitive to area type defects and more suitable for testing cracks caused by quenching, rolling, forging, casting, welding, plating, grinding and fatigue. There are several ways to display defects in magnetic detection. Some using magnetic particle and are referred as magnetic particle testing. Some methods that do not use magnetic particle are customarily called leakage magnetic testing, which often uses an induction coil, magnetic tube and Hall element to detect the defects; it is more hygienic than magnetic particle testing, but not as good as the former in intuition.

Next, we will discuss the eddy current NDT testing approach. It is observed that eddy current testing is typically implemented on tubes especially steam generator tubes [ref.]. The estimation of the parameters associated with defects from eddy current nondestructive testing data is an important tool to evaluate the structural integrity of critical metallic parts. In addition, most of the algorithms proposed involve some sort of Neural Network (NN) approach for classification. In these complex systems, the simultaneous and accurate measurement of more than two interdependent parameters is difficult using standard statistical regression analysis tools. Hence, artificial neural networks (ANNs) have been explored when dealing with the complex relation between inspection data and defect properties. For example, in [11] an in-service inspection of complex systems such as nuclear steam generator (SG) tubes and their surrounding support structure is tested. The pulsed eddy current data was obtained using a single driver with an array of eight pick-up coils configured for inspection of Alloy-800 SG tube fretting, accompanied by tube offset within a simulated corroding ferromagnetic support structure. They processed the time-voltage data by a modified principal component analysis (MPCA) to reduce data dimensionality, and these scores were fed into an ANN that simultaneously targeted four parameters associated with support structure, hole size, tube off-centering in two dimensions, and fret depth. Similarly, [12-13] have used ANN in addition to eddy current NDT for defect classification. Reference [12] proposes the use of principal component analysis (PCA), wavelet decomposition, and the discrete Fourier transform to extract relevant features used by the ANN. Feature extraction is based in the modeling of the testing data by a template of additive Gaussian functions and nonlinear regressions to estimate their parameters. An ANN is trained using features extracted from a synthetic data set obtained with finite-element modeling of the eddy current probe. Reference [13] proposes a method for the

reliable estimation of crack shape and dimensions in conductive materials using a suitable nondestructive instrument based on the eddy current principle and ANN system post processing. After the design and tuning stages, a performance comparison between the two-machine learning systems neural network and support vector machine (SVM) is done. A neural network mapping approach has been proposed by [18] for the inversion problem in eddy-current testing. They use PCA data transformation step, a data fragmentation technique and a data fusion approach to solve the inversion problem.

To continue on the topic of steam generator tubes testing, [14] propose an inspection and monitoring of support structures combined with preventative maintenance programs that can alleviate these effects using pulsed eddy current combined with principal components analysis (PCA). Conventional eddy current inspection technologies are extensively used for detecting and sizing indications from wall loss, frets at supports, cracks and other degradation modes in the tubes, as well as assessing the condition of support structures. However, these methods have limited capabilities when more than one degradation mode is present simultaneously, or when combined with fouling. In another example of eddy current NDT of thick ferromagnetic tubes where the average wall thickness is measured with an exciter coil. Reference [16] studies the effect of the excitation frequency and the distance between the coils on the detected signal sensitivity to the tube properties, as a basis for usage of pulsed eddy current (PEC). It is done to overcome the key drawbacks of such eddy current tools. Due to the continuous frequency spectrum and time separation of direct and remote zone signals, the pulsed eddy current allows simultaneous measurement of average wall thickness and inner diameter with one detector coil separated from the exciter by one to two tube diameters.

A few other applications where pulsed eddy current NDT is employed are discussed in [15, 17, 19, 20, 21]. In reference [15], a pulsed eddy current NDT scheme is introduced for testing aging aircraft wing. Due to collateral damage posed by current methods of crack detection that utilize bolt hole eddy current which requires fastener removal, [15] propose a NDT in which pulsed eddy currents are induced in the aluminum wing structure by a probe centered over a ferrous fastener. They record the response signals and analyze them using a modified principal components analysis to show separation of groups of PCA scores from fasteners with and without notches in the borehole. A cluster analysis method in the form of the Mahalanobis distance (MD) is used to obtain a relative distance measurement between scores associated with cracks from those without cracks. The use of multiple sensors in pulsed eddy-current detection for three-dimensional (3-D) subsurface flaw imaging is discussed in [17]. In order to eliminate the variations among Hall Effect based devices a normalization technique has been proposed in [17]. An orthogonal information extracted from a feature based principal component analysis method for multiple sensor fusion has been introduced here. 3D- flaws are reconstructed and measured by using the features of multiple projection coefficients obtained through these sensors.

Due to its features of abundant frequency, components and large exciting currents, pulsed eddy current NDT is preferred over eddy current NDT especially when it comes to reconstruction of stress corrosion cracks (SCCs). Hence [19] investigates stochastic optimization methods of neural network, simulated annealing and genetic algorithm to reconstruct the SCC profile from the pulsed eddy current signals. As seen in earlier examples pulsed eddy current NDT is a powerful inspection technique, reference [20] introduces a pulsed eddy current thermography to detect surface cracks. Pulsed eddy current thermography will allow the operator

to observe the heating developed from the eddy current distribution by using infrared imaging which in return detects defects over a relatively wide area in milliseconds. Reference [20] studies the effect of pulsed eddy current thermography on carbon fiber reinforced plastic (CFRP) materials. They have developed a system to observe the directional electrical conductivity of CFRP material by observing its heating pattern. They also study the position of the coil with respect to machined notches at different widths and depths in order to see its effect on normalized temperature rise and fall. Another example of pulsed eddy current thermography is described in [21]. As stainless steel is vital in numerous industries it is important to study the stainless steel weld which is its weaker part but plays an important role in structure integrity. Reference [21] introduces an independent component analysis to remove the influence of weld inhomogeneity which will play a key role in enhancing the defect information for pulsed eddy current thermography NDT.

The fourth method we discuss is laser based NDT. Typically, laser inspection is carried out in tubular structures like pipes. Reference [22] proposes a new noncontact laser-inspection technique to inspect the inner surface of mini-diameter pipes. It is based on a position-sensitive detector (PSD). It is carried out by projecting a light spot onto the pipe inner wall by reflecting the laser beam using two mirrors. This in return produces four current signals when the light spot is read by the 2-D PSD. The spot position on the inner wall can be calculated based on the magnitude of the current signals in a local 3-D coordinate system. The laser beam can scan the surface of the inner wall with the help of a micro motor. After that, data segmentation and least squares fitting algorithms are implemented on the co-ordinates of the sample points obtained to reconstruct the curve section. A mini-robot can inspect a long curved pipe and detect flaws in the inner surface of mini-diameter pipes. Along similar lines, [23-24] present a new sensing

methodology for the automated inspection of pipes. They use a transducer, which consists of a low-cost laser based profiler attached to the standard CCTV camera. Both [23-24] acquire images of the light projections on the pipe wall. However, the difference in these two approaches is that they use different techniques to analyze the image data acquired by these low cost laser based profilers. Reference [23] analyzes the image data based on differential processing leading to highly-noise tolerant algorithms with the subsequent application of artificial neural networks. While, [24] uses the intensity distribution from the acquired image and feed them to artificial neural network for fault detection. Similarly, authors in [25] propose a method to locate a spot on surface of a pipe in a 3D co-ordinate reference system by means of triangulation using the laser spot arrays in the camera data. Reference [26] introduces an infrared thermography based NDT using a thermal excitation from a CO_2 laser of 10.6m wavelength. Their work is primarily focused on finding defects in bio ceramics through thermal excitation. In order to achieve the thermal excitation, they focused the laser beam towards the material from vertical to horizontal direction. They used a temperature of a fault free sample as a basis to find the difference between the faulty sample and a fault free sample.

Finally, as seen from the previous examples, the industry is moving towards NDT of optical image analysis. In recent years, an accelerated trend in optical NDT is observed. An automated 3D optical measurement system is proposed in [29]. Typically, in industrial inspection, coordinate measurement machines (CMMs) provide accurate measurement but are very time consuming. The authors of reference [29] introduce a pixel- to- pixel sensor calibration which can acquire patch-by-patch data of an automotive part. This patch is further inspected for faults, which proves to save a lot of time. Optical NDT is majorly used to detect the surface flaws, whether it be pipes, wind turbine blades or automotive parts. Reference [27] studied that

detecting and quantifying cracks as small as hair thickness with optical imaging is feasible, and the orientation of a crack is not sensitive to the angle at which the inspection camera is set. By using the canny edge detector method, the threshold values was optimized which in return negated the uneven background illumination. It was observed that by taking intersection of images that are processed by sobel and canny edge detectors increases the accuracy of crack detection by reducing the noise. As the conventional NDTs are time consuming, [28] proposes a new NDT approach using digital image processing that can potentially decrease the inspection time. The image is analyzed in transform domain using the Discrete Cosine Transform (DCT) and Counterlet Transform (CT). Using iterative filter banks the 2D- spectrum is divided into fine slices by the Counterlet transform. The directional energy components of the decomposed sub-bands are recorded. These values are used to distinguish between the faulty and fault free part. On similar lines, in another approach of discrete cosine transform, the 2D- spectrum is divided into low and high frequency components. The first order moment of these components is calculated and recorded as feature vectors. In order to classify the part under test into a faulty or fault free part a correlation based classifier is used. Experimental results show significant improvement when discrete cosine transform is used over Counterlet transform. As seen in past few examples some of the image processing techniques used are typically used in algorithms like image retrieval or most recently in face recognition. Hence, authors of reference [30] decided to use face recognition algorithms to conduct optical NDT. The focus of the proposed methodology is on computational efficiency to ensure that the algorithm runs in real time in high volume manufacturing environments. The algorithm is trained with previously classified images. The images of part under test are then classified into two groups, faulty and fault-free. The authors of

reference [30] propose a method that combines Discrete Cosine Transform with Fisher's Linear Discriminant Analysis to detect faults such as surface breaking cracks.

1.2 Motivation of Thesis

The motivation of this thesis is to develop an algorithm, which can deliver high consistency as expected from an artificial intelligence technique while achieving a high defect detection rate. Although, various NDT modalities such as acoustic resonance, magnetic particle, laser scanning and eddy current testing are suitable techniques for testing, and have been implemented in industry, they can suffer from multiple drawbacks, including expensive equipment, susceptibility to noise, and the need to create a large database of good parts. As a result, our efforts have concentrated on non-contact, optical inspection, particularly since many critical flaws are surface flaws. Obviously, in optical inspection, the algorithm is only as good as the image captured. Similar to acoustic resonance testing, which flags faulty parts through analysis of the samples-under-test against a large database of good parts, the proposed optical technique relies on a database of recorded images. Although spatial domain image processing techniques are promising, they are susceptible to noise and tend to be less reliable than frequency domain techniques. This thesis concentrates on frequency domain image processing techniques with the following unique contributions:

1. Design of a robust 2-D discrete wavelet and rotated wavelet function capable of implementing any wavelet (for e.g. Debauchies, Symlets, Biors, ReverseBiors, etc.) for feature extraction.

2. Formulation of an algorithm, which uses DWT along with KNN classifier for automatic optical inspection of cast iron automotive part. The algorithm can be modified easily depending upon the part under test.

3. Design of a new image acquisition system in the form of shape from polarization. The algorithm reconstructs the part from a partially linearly polarized light reflected from the part. After reconstruction, using the image to classify the part under test into acceptable and faulty.

1.3 Thesis organization

This thesis is organized into six chapters. Chapter 2 introduces the theory required to understand the concept of wavelet transform. Chapter 3 discusses the classifier used in the form of K- nearest neighbor to classify the part under test. Chapter 4 presents the experimental approach proposed in this thesis. The experimental results are discussed in chapter 5. Finally, in chapter 6 we conclude the thesis and provide an outlook on future work.

Chapter 2 Wavelet Transform

Wavelet transform is a mathematical technique used in signal analysis for decomposing functions hierarchically. A wavelet is a small-localized wave of a particular shape and finite duration that has an average value of zero [31]. The wavelet transform is a tool that cuts up data, functions, or operators into different frequency components, and then studies each component with a resolution matched to its scale. Representing any function $f(x)$ as a superposition set of basis functions is the main idea behind wavelets. The advantage of the transform is that the band of analysis can be fine adjusted so that high frequency components and low frequency components can be detected precisely. Results of the wavelet transform are shown on both the time domain and the frequency domain. The wavelet transform, which has a change in the analysis scaled by the factor of two, is called discrete wavelet transform (DWT). The DWT is an implementation of the wavelet transform using a discrete set of the wavelet scales and translations obeying some defined rules. In other words, this transform decomposes the signal into mutually orthogonal set of wavelets, which is the main difference from the continuous wavelet transform (CWT). Images are represented at different resolutions for various frequency bands. Discrete Wavelet Transform provides efficient computation algorithm and sparse representation of an image, which are important aspects in any classification scheme.
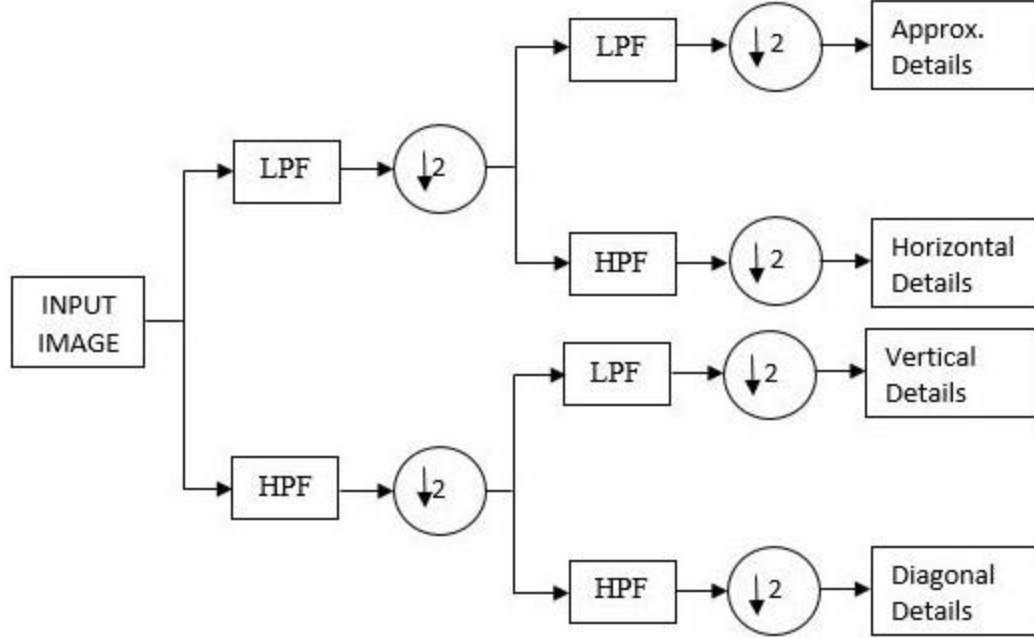
Fig. 2.1. Analysis of the 2-D Discrete Wavelet Transform (DWT).

2.1 Concept of 2D-Discrete Wavelet Transform

Unlike the Fourier transform, the DWT offers better frequency selectivity by using a short analysis window for low frequency, and a long analysis window for high frequency. The 2D-DFT is given by [37]:

$$F(u, v) = \frac{1}{lm}\sum_{x=0}^{l-1} \sum_{y=0}^{m-1} f(x, y)e^{-j\omega t} \tag{2.1}$$

The basis of discrete wavelet transform is modified to $e^{-j(\omega_1 t_1 + \omega_2 t_2)}$ from $e^{-j\omega t}$. The 2D discrete wavelet transform is a two variable function. The two variables are scaling and wavelet function denoted as $\varphi(x)$ and $\psi(x)$, respectively [32]. The $\psi(x)$, also called mother wavelet, is given by:

$$\Psi_{l,m}(x) = 2^{-l/2} \psi(2^{-l/2} x\text{-}m) \tag{2.2}$$

The wavelet coefficients of an arbitrary signal $f(x)$ can be determined easily due to its orthonormal property using the following equation [33]:

$$C_{l,m} = \int_{-\infty}^{+\infty} f(x)\psi_{l,m}(x)dx \tag{2.3}$$

15

In order to get the mother wavelet ψ (x), we must first determine the scaling function $\varphi(x)$,

$$\varphi(x) = \sqrt{2}\sum_n h(n)\varphi(2x-n)$$

(2.4)

Here, $h(n)$ are expansion coefficients. This leads us to the wavelet function $\psi(x)$, which is related to the above scaling function $\varphi(x)$ as follows:

$$\Psi(x) = \sqrt{2}\sum_n g(x)\varphi(2x-n)$$

(2.5)

where, $g(x) = (-1)^n h(1-n)$.

In order to have the set of basis functions described in (2.2) orthonormal and unique, the *h(n)* coefficients need to meet several conditions as mentioned in [36, 37]. Here, the *g(n)* and *h(n)* represent the low pass and high pass filter coefficients, respectively.

The 2D- Discrete wavelet transform is designed using non-separable 2D filters in order to get good frequency response. It is difficult to design a non-separable filter, but an alternative to it is taking a tensor product of scaling and wavelet function. As the wavelet function is separable, it can be represented as *f(x,y)= f1(x)f2(y)*. The scaling function $\varphi(x, y)$ represents the low frequency components. Hence, only one scaling function is present. There are three different types of wavelet functions $\psi_h(x,y)$, $\psi_v(x,y)$, and $\psi_d(x,y)$. These three wavelet functions are related to the order in which the filters (i.e. low pass and high pass) are applied. Hence, the corresponding 2D-filter coefficients can be determined as:

$\varphi(x, y) = \varphi(x) \varphi(y)$ (2.6)

$\psi_h(x,y) = \varphi(x) \psi(y)$ (2.7)

$\psi_v(x,y) = \psi(x) \varphi(y)$ (2.8)

$\psi_d(x,y) = \psi(x) \psi(y)$ (2.9)

Fig. 2.2. Original image of the sample on which 2D- Discrete Wavelet Transform is implemented.
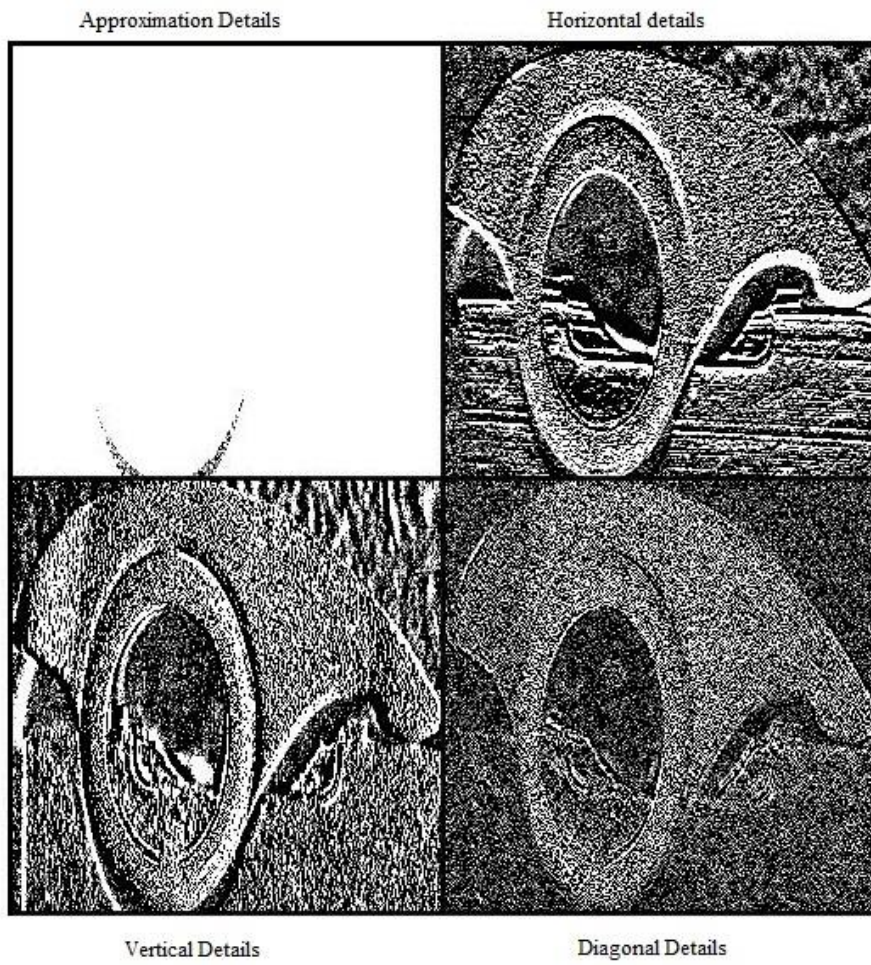
Fig. 2.3. 2D- Discrete Wavelet Transform image decomposition (1st level).

This results in decomposition of a two dimensional signal into four sub-bands viz. approximation details (LL), horizontal details (LH), vertical details (HL), and diagonal details (HH). Fig. 2.3 presents the 2-D Discrete Wavelet Transform decomposition of an image. The approximation details are achieved by low pass filtering in both x and y direction. The horizontal details are achieved by low pass filtering in x direction and high pass filtering in y direction. The vertical details are obtained by applying high pass filter in x direction and low pass filter in y direction. Finally, the diagonal details are obtained by applying high pass filter in both x and y direction. Generally, 2D-DWT is implemented on images, so the x and y direction correspond to rows and columns respectively. It is now clear that a 2D-discrete wavelet transform is implemented in two stages by using 1D- discrete wavelet filters (DWF) first on rows and then columns. The 2D-discrete wavelet transform decomposition is implemented in two steps as demonstrated in Fig. 2.1. This has similarities with the pyramid algorithm of the Fast Fourier Transform (FFT) [34, 35]. The DWT provides edge information along orientations, which are horizontal detail coefficients (LH), vertical detail coefficients (HL), and diagonal detail coefficients (HH), respectively. The sub-band characteristics in the 2D frequency domain is idealized in Fig. 2.4.
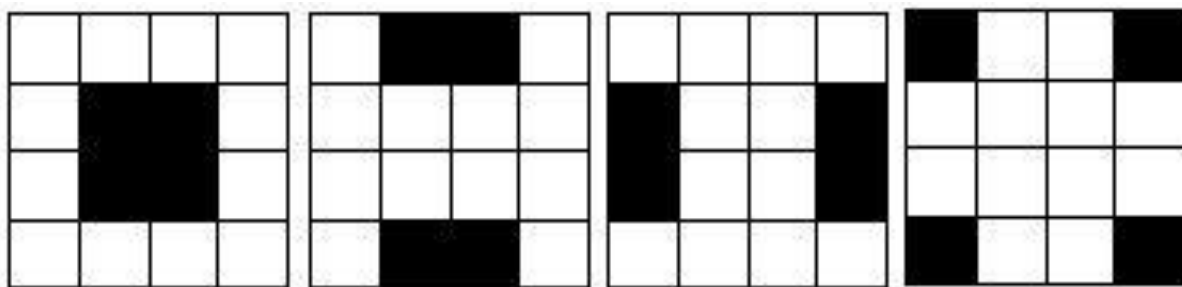
Fig. 2.4. Idealized wavelets (LL, LH, HL, HH) in 2D- frequency domain (origin is at the center).

2.2 Disadvantages of 2D-Discrete Wavelet Transform

The DWT suffers from four intertwined complexities despite its ability to provide multiresolution representation. First, the wavelets being band-pass functions are shift invariant, i.e. a small shift will result in oscillations around singularities. The effects of these drawbacks are typically observed in signal processing applications [38, 40]. Second, wavelets have aliasing effects due to discrete down-sampling after convolution of low pass filter coefficients and high pass filter coefficients. The aliasing effect can be cancelled out by using reconstruction filter coefficients but they are used to recreate the image and cannot provide feature extraction [39, 40]. Third, discrete wavelet transform has lack of directionality i.e. it can only provide edge information along $0°, 90°, \pm45°$ orientation [40]. In addition, it does not provide any phase information. Finally, the edge information, especially along the $\pm45°$ orientation, demonstrates checkerboard artifacts [40, 41], as depicted in Fig. 2.4.

2.3 Concept of 2D-Rotated Wavelet Transform

In the previous section, we discussed some of the drawbacks that make 2D-DWT classification applications less efficient. Hence, in order to improve upon those drawbacks a new set of discrete wavelet filters are generated by rotating the standard 1D wavelet filters by $\pm45°$. Each sub-band generated after applying the Rotated Wavelet Filter (RWF) covers a quarter of the total frequency range [43]. The 2D-RWT maintains the orthogonality property from the 2D-DWT as the following condition holds true [42]:

$$\frac{1}{2\pi} \int_{-\infty}^{\infty} h_i(w)\overline{h_j(w)}dw \quad = \quad 0, \quad where \quad (i \neq j)$$

$$(2.10)$$

Here, $h_i(\omega)$ is the Fourier Transform. The size of the new 2D-RWF set is (2N-1) x (2N-1), where N is the size of 1D-DWF [41]. Figure 2.5 shows the corresponding 2D-RWF set generated from the conventional 1D-DWF set. The subscript 'r' on the sub-bands denotes that they correspond to the RWF set. Figure 2.6 shows the sub-band characteristics of 2D-RWT in the frequency domain. The rotation by $\pm45°$ is performed on the 1D-DWF in order to negate the checkerboard artifact while aliasing is not observed, as there is no discrete down sampling. Hence, the 2D-RWT addresses the shortcomings of the 2D-DWT mentioned in the previous section.

			4			
		3		8		
	2		7		12	
1		6		11		16
	5		10		15	
		9		14		
			13			

(a)

	LL_r	LH_r	HL_r	HH_r
1	L_1L_1	L_1H_1	H_1L_1	H_1H_1
2	L_2L_1	L_2H_1	H_2L_1	H_2H_1
3	L_3L_1	L_3H_1	H_3L_1	H_3H_1
4	L_4L_1	L_4H_1	H_4L_1	H_4H_1
5	L_1L_2	L_1H_2	H_1L_2	H_1H_2
6	L_2L_2	L_2H_2	H_2L_2	H_2H_2
7	L_3L_2	L_3H_2	H_3L_2	H_3H_2
8	L_4L_2	L_4H_2	H_4L_2	H_4H_2
9	L_1L_3	L_1H_3	H_1L_3	H_1H_3
10	L_2L_3	L_2H_3	H_2L_3	H_2H_3
11	L_3L_3	L_3H_3	H_3L_3	H_3H_3
12	L_4L_3	L_4H_3	H_4L_3	H_4H_3
13	L_1L_4	L_1H_4	H_1L_4	H_1H_4
14	L_2L_4	L_2H_4	H_2L_4	H_2H_4
15	L_3L_4	L_3H_4	H_3L_4	H_3H_4
16	L_4L_4	L_4H_4	H_4L_4	H_4H_4

(b)

Fig. 2.5. Set of wavelet filter coefficients for tap 4. (a) 2D- RWT filter structure (empty cells are replaced by zero); (b) The coefficient values for each parameter. *Note: Here L stands for low pass filter coefficients, while H stands for high pass filter coefficients.*
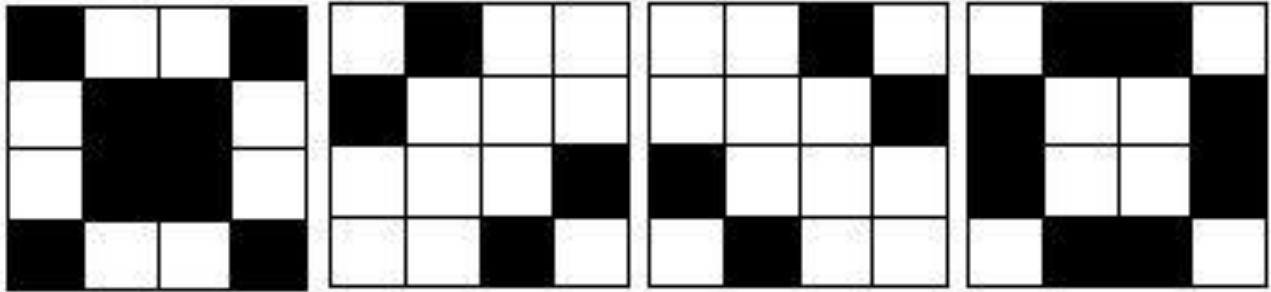
Fig. 2.6. Sub-band characteristics for 2D Rotated Wavelet Transform.

Chapter 3 K-Nearest Neighbor Classifier

3.1 Concept of K- Nearest Neighbors

One of the simplest decision procedures that can be employed for classification is the nearest neighbor (NN) rule. It classifies a sample based on the category of its nearest neighbor. When large samples are involved, it can be shown that this rule has a probability of error which is less than twice the optimum error. Hence, there is less than twice the probability of error compared to any other decision rule. The nearest neighbor based classifiers use some or all the patterns available in the training set to classify a test pattern. These classifiers essentially involve finding the similarity between the test pattern and every pattern in the training set.

The K-nearest neighbor (KNN) is a special case of the nearest neighbor classifier [44]. In this algorithm, instead of finding just one nearest neighbor as in the nearest neighbor's algorithm, k neighbors are found. The majority class of this k nearest neighbors is the class label assigned to the new pattern. The KNN classifier is very powerful and reliable classifier when it comes to machine learning algorithm. Its functionality is based on finding the nearest neighbour to a particular vector from a given set of vectors.

The Class Based KNN (CB-KNN) is a somewhat different KNN extension [45]. It was developed because the datasets are often unbalanced in regards to their class structure, so it may be the case that one class has too few elements to "win" the vote of a classification of the KNN classifier. The CB-KNN algorithm deals with these datasets working in the following way: for every test element, the K nearest elements of each class are taken. Afterwards, the harmonic mean of the distances of these neighbors is calculated (so that it is not influenced so much by the

most distant elements). Finally, these means are compared and the class yielding the lowest value is chosen for the classification.

In KNN classifier, we have to provide three classes that is sample, training and group, where sample contains the query image feature matrix, training contains the database image feature matrix and the group contains various groups into which query image is to be classified. There are various distance metrics available, which will help the KNN classifier to classify the query image into one of the groups. The four most common distance metrics used are labelled as follows [39]:

1. Euclidean Distance

2. City block Distance

3. Cosine Distance

4. Correlation Distance

1. EUCLIDEAN DISTANCE

In mathematics, the Euclidean distance or Euclidean metric is the "ordinary" (i.e. straight-line) distance between two points in Euclidean space. With this distance, Euclidean space becomes a metric space. The associated norm is called the Euclidean distance. The Euclidean distance eqn. is given by:

$$D_E[(u, v)] = \sqrt[2]{[(v_1 - u_1)^2 + (v_2 - u_2)^2]} \tag{3.1}$$

where,

u= (u1, u2….un)….Database image feature vector matrix.

v= (v1, v2….vn)….Query image feature vector matrix.

2. CITYBLOCK DISTANCE

It is a form of geometry in which the usual distance function of metric or Euclidean

geometry is replaced by a new metric in which the distance between two points is the sum of the absolute differences of their Cartesian coordinates. The City block distance eqn. is given by:

$$D_{Ct}(u, v) = \sum_{i=1}^{n}|u_i - v_i|$$ (3.2)

where,

u= (u1, u2….u$_n$)….Database image feature vector matrix.

v= (v1, v2….v$_n$)….Query image feature vector matrix.

3. *COSINE DISTANCE*

Cosine distance is a measure of similarity between two vectors of an inner product space that measures the cosine of the angle between them. The cosine of 0° is one, and it is less than one for any other angle. It is thus a judgement of orientation and not magnitude: two vectors with the same orientation have a cosine similarity of one, two vectors at 90° have a similarity of zero, and two vectors diametrically opposed have a similarity of -1, independent of their magnitude. Cosine distance is particularly used in positive space, where the outcome is neatly bounded in [0, 1]. The Cosine distance eqn. is given by:

$$u.v = \|u\| \|v\| \cos \theta$$ (3.3)

The cosine distance between vectors u and v, are computed by the dot product and its magnitude [46].

Here,

u is Database image feature vector matrix.

v is Query image feature vector matrix.

4. *CORRELATION DISTANCE*

Correlation distance is a measure of statistical dependence between two random variables or two random vectors of arbitrary, not necessarily equal dimension. An important

property is that this measure of dependence is zero if and only if the random variables are statistically independent. This measure is derived from a number of other quantities that are used in its specification, specifically: distance variance, distance standard deviation and distance covariance. The correlation distance is given by:

$$D_{Cor}(u,v) = [(d_{Cov}(u,v))/\sqrt{d_{Var}(u) * d_{Var}(v)}] \tag{3.4}$$

The correlation distance is calculated by dividing the distance covariance by product of distance standard deviation of u and v.

In Eq, (3.4) we denote,

u as the database image feature vector matrix.

v as the query image feature vector matrix.

3.2 Comparison between K-Nearest Neighbors and K-Means

These are two completely different methods. The fact that they both have the letter K in their names is a coincidence. K-means is a clustering algorithm that tries to partition a set of points into K sets (clusters) such that the points in each cluster tend to be near each other. It is unsupervised because the points have no external classification. K-nearest neighbor's is a classification (or regression) algorithm that in order to determine the classification of a point combines the classification of the K nearest points. It is supervised because you are trying to classify a point based on the known classification of other points. However, some algorithms have explored the possibility of for feature learning using K-means [47].

Chapter 4 Experimental Approach

Our proposed model consists of three parts: 1) Sample Acquisition, 2) Feature Extraction, and 3) Sample Classification. In this chapter, we present two procedures. In the first procedure, the images are acquired using a high-resolution RGB camera, while the feature extraction is done in the transform domain. The measures taken to obtain high quality images for accurate classification are discussed in the subsequent sections. Once the image is acquired, we follow an algorithm as outlined in Fig. 4.1. The indexing algorithm provides us with feature vectors required for classifying the part-under-test (PUT) into either acceptable or faulty bins. These feature vectors are obtained by applying frequency domain technique such as discrete wavelet transform (DWT) and rotated wavelet transform (RWT). These feature vectors are stored in a vector format, which is called as feature vector matrix (FVM). The testing algorithm applies the same transform that was applied during indexing for feature extraction of PUT. Using the FVM, the PUT is classified into acceptable or faulty bins by the KNN classifier. In a second procedure, the images are acquired using a gray scaled camera with a polarizer placed in front. In this approach we consider the effect of polarization and surface conditions of the part. The polarizer is rotated in steps of 45° and images are captured simultaneously. A phase image is reconstructed which will have no effect on illumination or surface condition. A database of phase images of fault free parts is created and the PUT is tested by taking the variance between the PUT and mean of the phase images of fault free parts in database. The following subsections describe every aspect of the algorithms in detail.
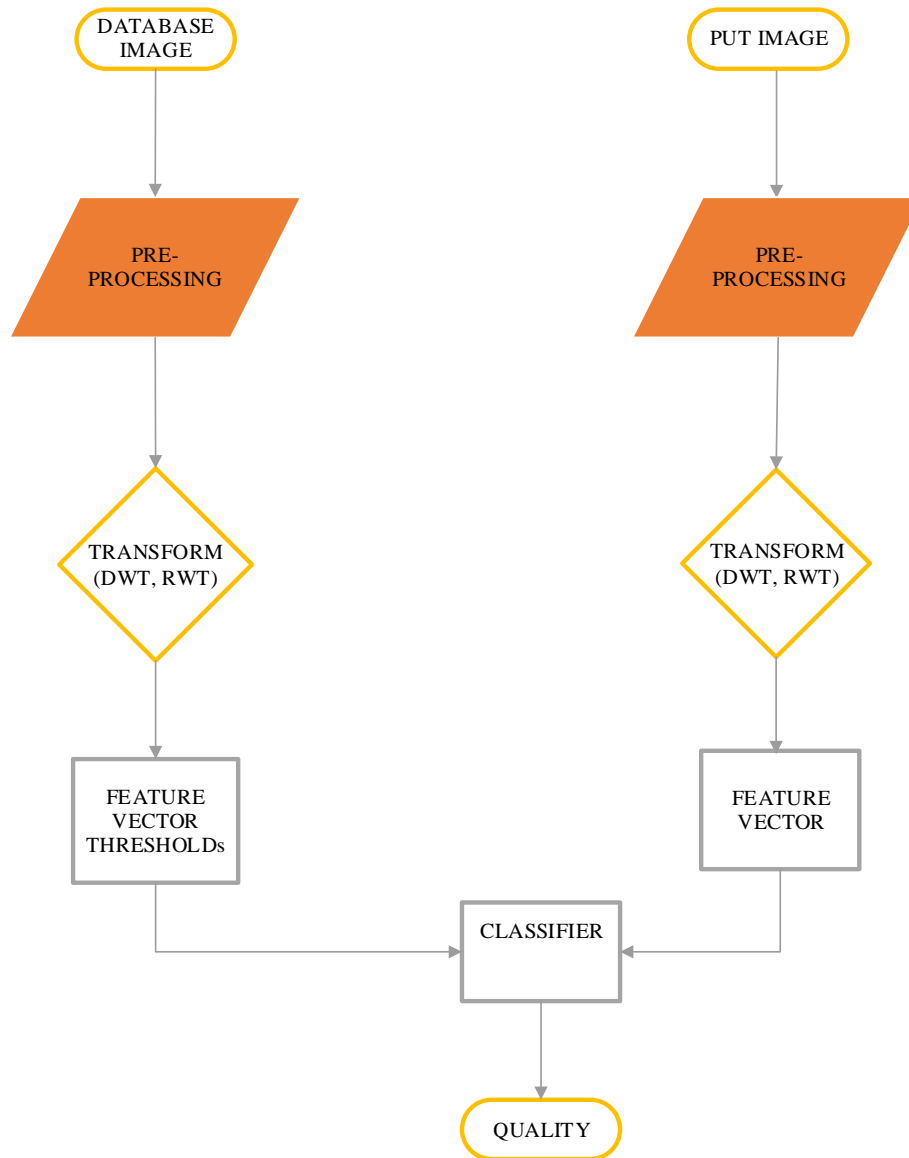
Fig. 4.1. Indexing and testing algorithm for first procedure of sample classification.

4.1 Sample Acquisition

4.1.1 RGB camera approach

The image acquired from the RGB camera is of dimension 3264 x 1836 pixels. The wavelet transform decomposes an image into four sub-bands, which are half the dimension of the image. Hence, the algorithm resizes the image to the nearest square matrix of order 2n without

approximating (i.e. replicating or padding) the boundary pixels. Also the size of the part is approximately 3in x 1.5in, hence resizing the input image into 1024 x 1024 pixels will result in a pixel width of 16 microns, which provides excellent resolution. However, the images acquired are in RGB scale and implementing a wavelet transform on every scale will increase the computation time without having any significant advantage over gray scale as seen in Fig. 4.2.
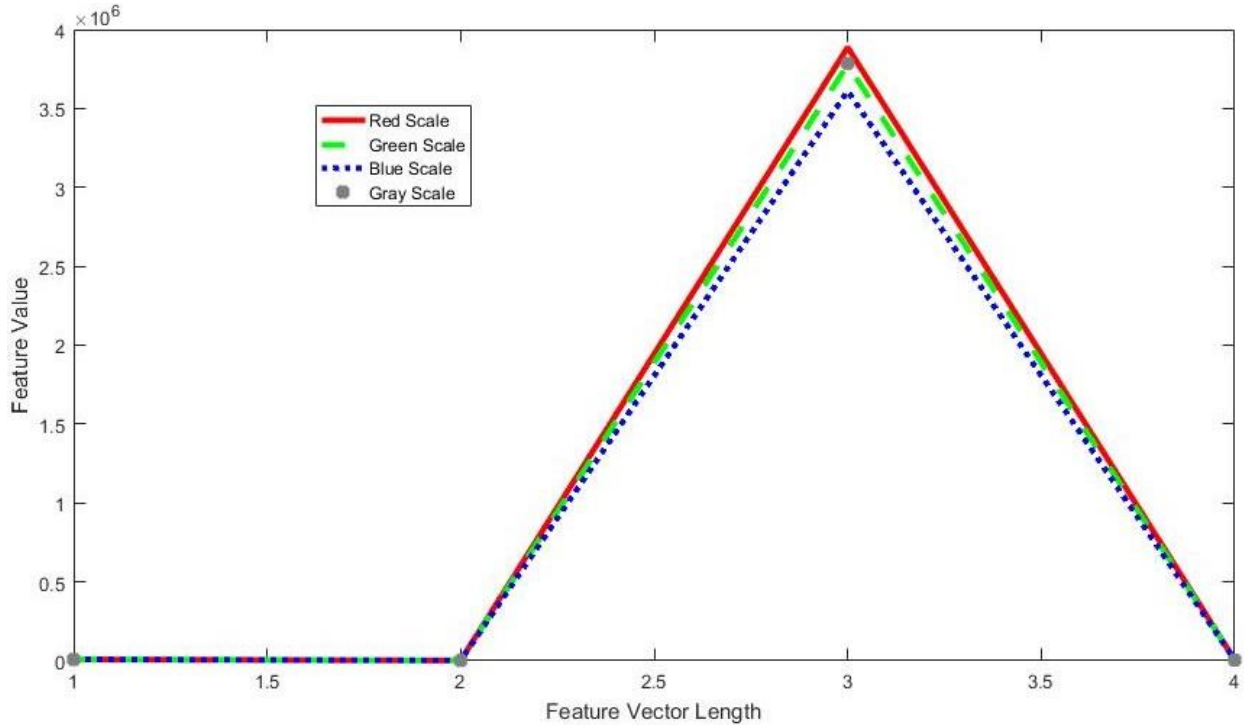
Fig. 4.2. Feature value comparison between gray scale and RGB scale.

The database is composed of 100 images of 100 different parts acquired under ambient lighting with a 22.0 megapixel camera. These 100 images are used as part of the indexing algorithm described in Fig. 4.1, since the quality (i.e. faulty or acceptable) was known beforehand. The indexing database is then divided into two bins (faulty and acceptable) with each bin having 50 images of 50 independent parts for threshold generation. Fig. 4.3a shows a random sample from the faulty bin while Fig. 4.3b shows the image of an ideal, fault free part from the acceptable bin.

Fault (Hole)

Fault (Excess Metal)

(a)

(b)
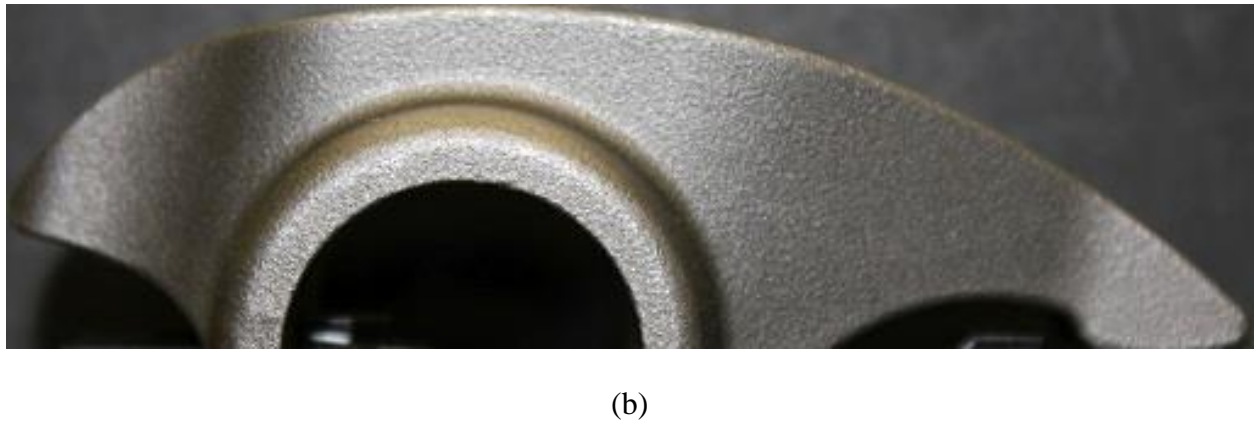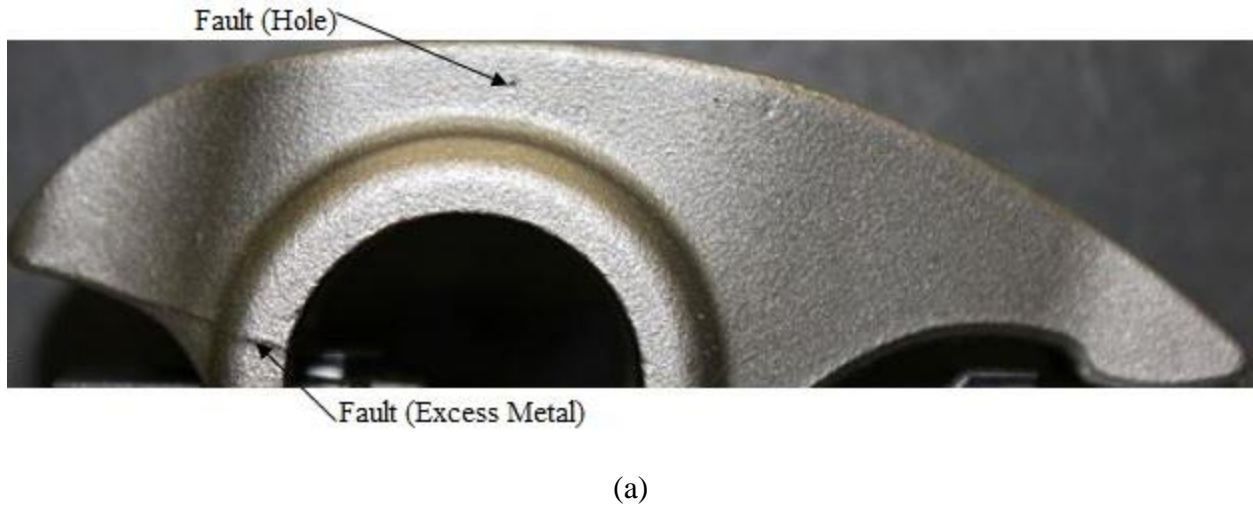
Fig. 4.3. Images used in an indexing algorithm. (a) Sample of a fault observed in the faulty part database. (b) Sample of a fault free surface observed in the acceptable part database.

4.1.2 Shape from polarization approach

A new way of image acquisition in the form of the shape reconstruction from polarization is explored in this section. There are two steps involved in shape reconstruction from the polarization method. First, we have to calculate the surface normal using the properties of light reflection. Second, we have to reconstruct the 3D object by integrating the surface normal.

1. Polarized Imaging

We exploit an important property of a reflected light, which implies that an un-polarized light becomes partially linearly polarized after reflection and depending upon the surface normal

and its refractive index. There are three parameters in a partially linearly polarized light: light magnitude (I), degree of polarization (ρ), and angle of polarization (φ). Here the degree of ρ varies from 0 to 1 for completely un-polarized light and perfectly polarized light, respectively. We are using a rotating polarizer to study the relationship between the magnitude of the partially linearly polarized light wave (I_p) and the angle of the polarizing filter (α). According to [51], the above relationship can be given using a sinusoid:

$$I_p(\alpha) = \frac{I_{max}-I_{min}}{2}\cos(2\alpha - 2\varphi) + \frac{I_{max}+I_{min}}{2} \qquad (4.1)$$

Here I_{min} and I_{max} represent the minimum and maximum magnitudes seen through the polarizer, respectively. The sole purpose of polarization is to calculate the three parameters: light magnitude (I), degree of polarization (ρ), and angle of polarization (φ). As there are three parameters, we are required to take a minimum of three images from three different orientations. In this experiment we took eight images with a step of 45° between them.

The degree of polarization can be expressed as follows [51]:

$$\rho = \frac{F_o - F_p}{F_o + F_p} \qquad (4.2)$$

Here F_o and F_p are the Fresnel coefficients of reflection and are given by the ratio between the amplitude of the light reflected and incident light as per the plane perpendicular and plane parallel to the plane of incidence respectively. The Fresnel coefficients are given by the following formula:

$$F_o = \left|\frac{\sin(\theta_i-\theta_{rt})}{\sin(\theta_i-\theta_{rt})}\right|^2 , \quad F_p = \left|\frac{\tan(\theta_i-\theta_{rt})}{\tan(\theta_i+\theta_{rt})}\right|^2 \qquad (4.3)$$

where θ_{rt} and θ_i are angle of refraction and angle of incidence respectively. From reference [51], it is concluded that the parallel component F_p is smaller than the orthogonal component F_o. Hence, according to the plane of incidence the un-polarized light becomes partially linearly

polarized light. Therefore, it can be concluded

$$\emptyset = \varphi \pm \frac{\pi}{2} \quad , \text{where } \emptyset \text{ is the azimuth angle} \tag{4.4}$$

From the Snell-Descartes law the degree of polarization can be expressed as [48, 49]:

$$\rho(\theta_r) = \frac{2n \tan \theta_r \sin \theta_r}{\tan^2 \theta_r \sin^2 \theta_r + |\hat{n}|^2} \tag{4.5}$$

2. Surface Reconstruction

Once we acquire the reflection angle θ_r and the azimuth angle, $\emptyset$, we can compute the components of the surface normal according to:

$$\vec{n} = \begin{pmatrix} -\frac{df(x,y)}{dx} \\ -\frac{df(x,y)}{dy} \\ 1 \end{pmatrix} = \begin{pmatrix} p = \tan \theta_r \cos \emptyset \\ q = \tan \theta_r \sin \emptyset \\ 1 \end{pmatrix} \tag{4.6}$$

We use the Frankot – Chellappa [50] algorithm to reconstruct the surface by using the components of the normal as stated in Eq. (4.6). We can take the inverse Fourier transform of Eq. (4.7) to reconstruct the surface shape. Here, $\tilde{f}, \tilde{p}, \tilde{q}$ are the Fourier transforms of the surface height, and the x, y gradients, respectively.

$$\tilde{f}(u,v) = \frac{-ju\tilde{p} - jv\tilde{q}}{u^2 + v^2} \tag{4.7}$$

We employ the arrangement shown in Fig. 4.4 to acquire the images using a liquid crystal polarizer in front of a camera. In order to have uniform diffusion of light from all directions we used a white light tent and external light sources from bottom as seen in Fig 4.4. The liquid crystal polarizer is attached in front of the camera and is rotated eight times manually in steps of 45º.

Fig 4.4. Test setup for shape from polarization experiment.

The image is captured and stored for each angle of polarization. Figure 4.5 demonstrate the algorithm used for reconstructing the images. Fig 4.6 (a-c) demonstrate the reconstructed images using shape from polarization algorithm. These images constitute of optical images, magnitude image and phase image. The only difference between the optical and the magnitude image is that the magnitude image does not depend on illumination. In our classification approach, we use phase image to determine if the part poses any faults as it depends purely on geometric contrast. In other words, the phase image of all fault free parts will be identical. On other hand, the faulty part will have geometric abnormalities in the form of pitting or excess metal, which now can be clearly distinguished from fault free part. Figure 4.7 (a-b) shows the phase image of faulty and fault free part, respectively.
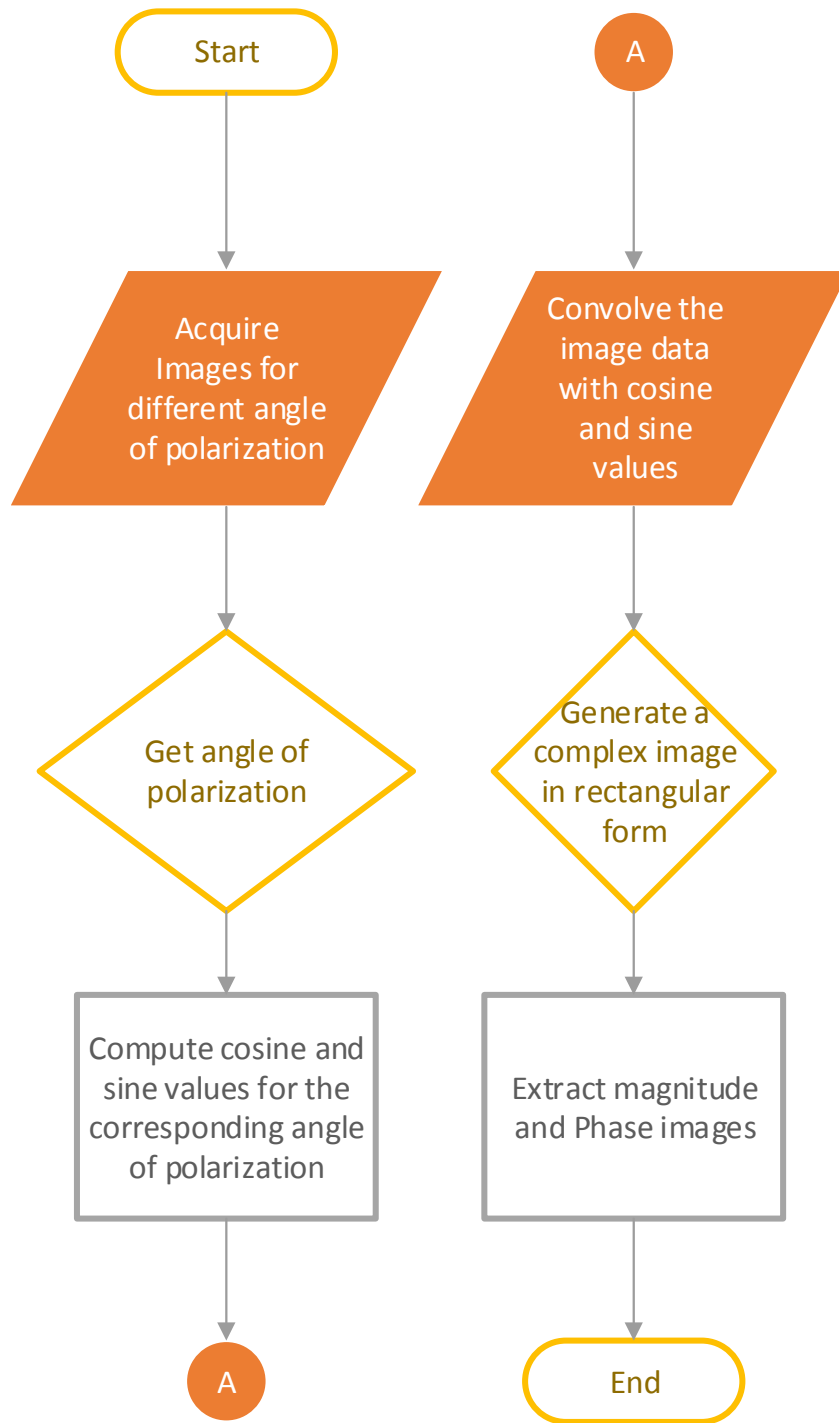
Fig 4.5. Algorithm used to reconstruct the images acquired using shape from polarization approach.

(a)

(b)

34
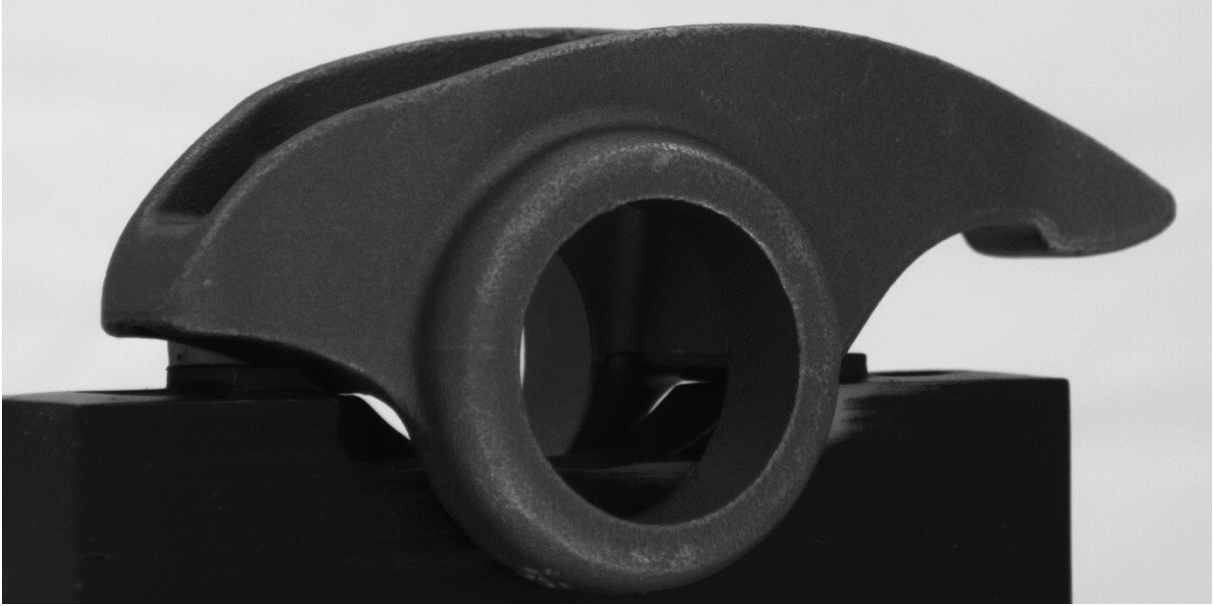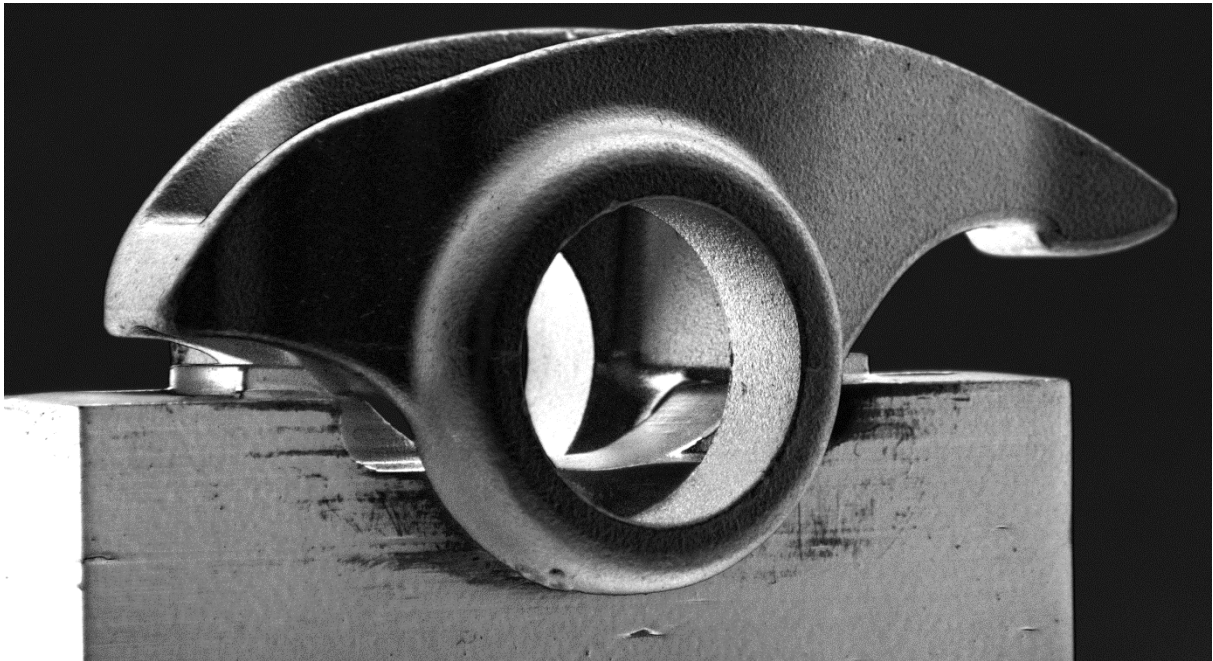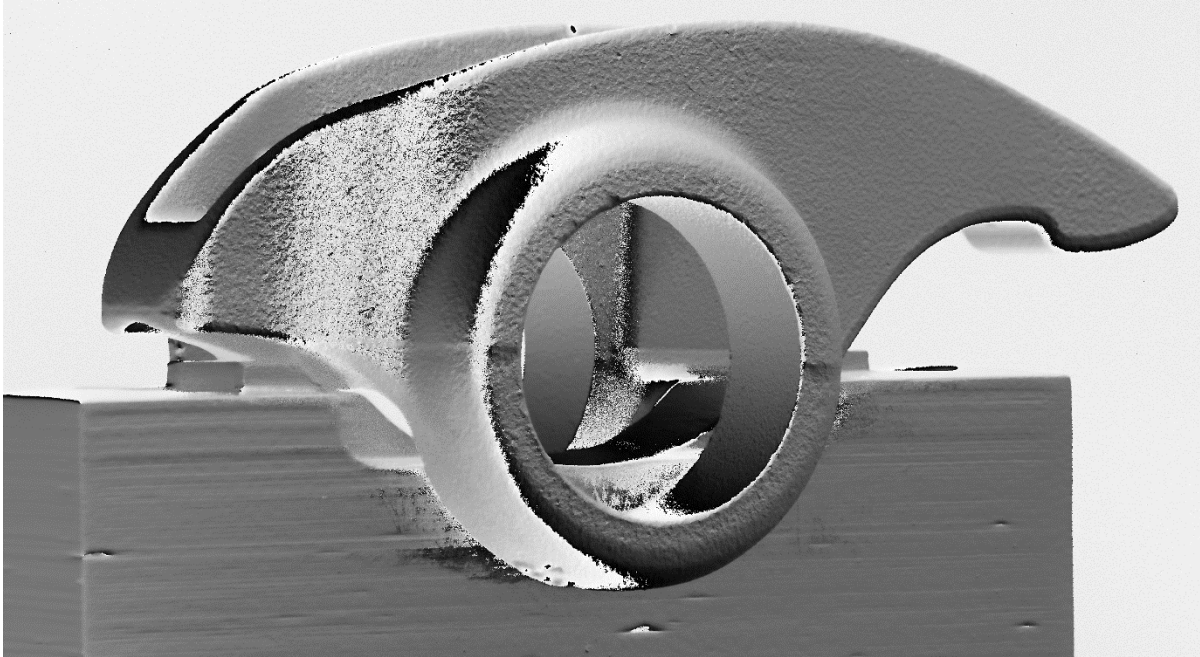
(c)

Fig. 4.6. Reconstructed images using the shape from polarization algorithm. (a) Optical image, (b) Magnitude image, (c) Phase image.
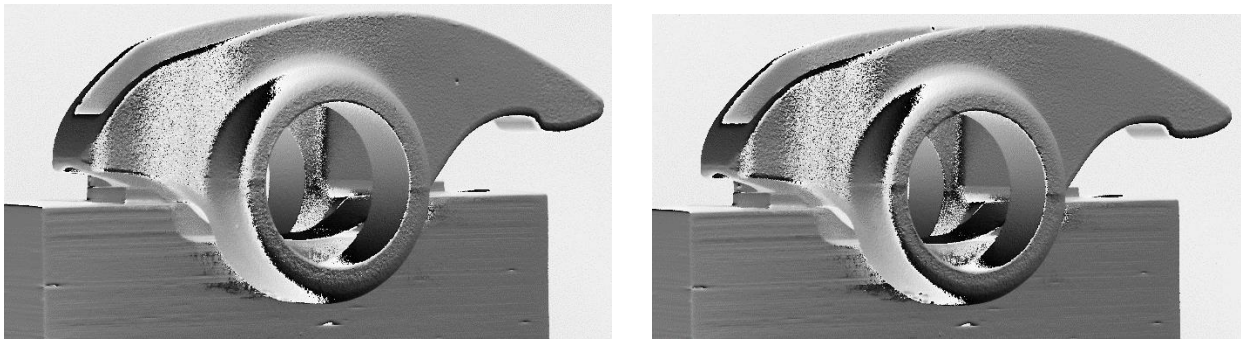
(a)   (b)

Fig. 4.7. Phase images from the dataset. (a) Sample of a phase image of the faulty part. (b) Sample of a phase image of a fault free surface.

4.2   Feature Extraction in Transform Domain

After pre-processing the indexing database images, the next step is to apply the 2D-wavelet transform to extract features. As explained in chapter 3, the wavelet transform

decomposes an image into four coefficients: approximation coefficients (LL), horizontal coefficients (LH), vertical coefficients (HL), and diagonal coefficients (HH). However, as the approximation coefficients contain low pass information and not edge information, this does not help us in the classification process. Nevertheless, if approximation coefficients are treated as an image, we can still obtain edge information by applying the DWT on those coefficients. This DWT approach on the approximation coefficients is called level decomposition. For level decomposition, it is important to resize the image into a square matrix of 2's order to reduce the aliasing effect, which occurs when down sampling is performed. Since the image is resized to 1024 x 1024 pixels during pre-processing, the level decomposition can be performed up to a maximum of 10 levels. After the 10th level, the resulting coefficients will be of size 1 x 1. The implementation of level decomposition is seen in Fig. 4.8.

The features extracted by applying DWT are an array of horizontal coefficients, vertical coefficients and diagonal coefficients. For an image of size 1024 x 1024, the LL, LH, HL, and HH coefficients will be of size 512 x 512 each after the first level decomposition and it will decrease by a factor of two after each level. Finally, after the 10th level the size of each coefficient will be 1 x 1. A feature vector matrix (FVM) is created (which is exclusive for each image) as demonstrated in Fig. 4.9. Each FVM consists of 30 feature elements (LH, HL, and HH of every level) and each feature element is approximated to size 1 x 1 (by taking the mean) in an effort to reduce the computational complexity. The rotated wavelet transform is implemented in similar fashion with minor changes. As described in previous chapters, the filter bank is generated by rotating the existing 1D-discrete wavelet filter set by 45°. The 2D-RWT addresses the shortcomings of the 2D-DWT. For example, the aliasing effect is not observed, as there is no discrete down sampling. However, as there is no down sampling, level decomposition cannot be

performed using the rotated wavelet transform. From Fig 2.5 in Chapter 2, it can be observed that if down sampling is performed, then all the non- zero elements after feature extraction will be discarded. Hence, the FVM for the 2D-RWT has only four values corresponding to LL, LH, HL, and HH. As wavelet transform is not confined to a single filter bank, there are many types of wavelets such as Debauchies, Symlets, Biorthogonal splines, Reverse biorthogonal splines, etc. In this experiment, the algorithm implemented 10 Debauchies (DB1-DB10), 10 Symlets (Sym2-Sym11), 10 Biorthogonal splines (Bior1.1- Bior3.5), and 10 Reverse biorthogonal splines (Rbio1.1-Rbio3.5) for feature extraction.

Once the FVM is obtained for each image in both bins, a threshold level is generated by taking the mean of all FVMs (element-by-element) in that bin. The threshold created for the acceptable and the faulty bins are called acceptable and fault threshold, respectively, and they consist of 30 elements each. These thresholds are then given to the testing algorithm, which classifies the PUT using KNN classifier as shown in Fig. 4.1. A part in the testing algorithm follows the same procedure as any part in the indexing algorithm, up to the FVM generation. Once the FVM is generated for PUT, it is then compared with the threshold levels using KNN and classified accordingly. The parts used in the testing algorithm are different (i.e. not a subset of the indexing database images) from those used in the indexing algorithm.

In most fault detection schemes, there is a high risk of false detection. This in turn reflects poorly on one's confidence over the fault detection scheme. Hence, it is equally important to pay attention to reducing the false detection percentage as it is to increasing the accurate detection percentage. False detection occurs if the features are at the opposite end of the appropriate threshold for that PUT or they are relatively close to (somewhere in between acceptable and faulty threshold) an inappropriate threshold for that PUT.
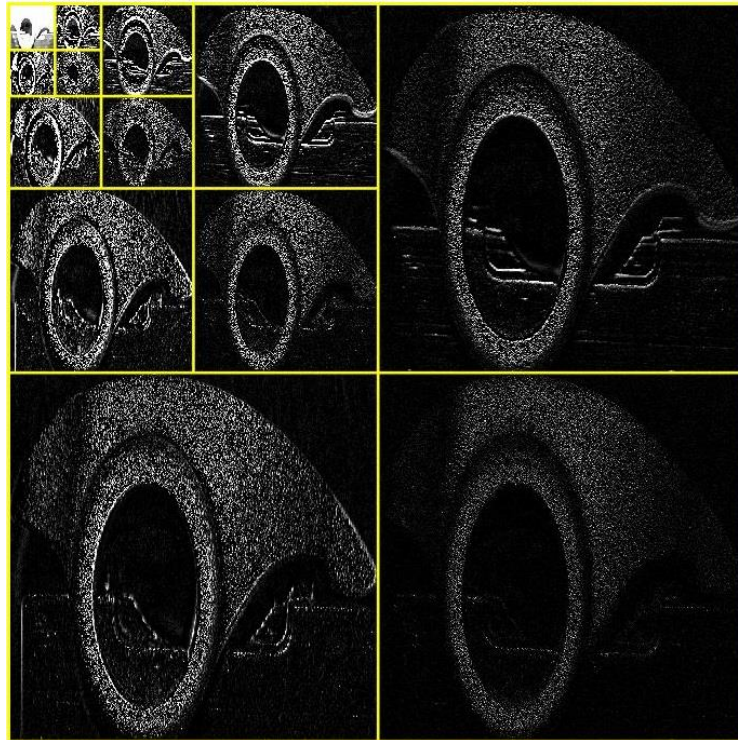
Fig. 4.8. Feature vector generation after 2-D DWT decomposition.
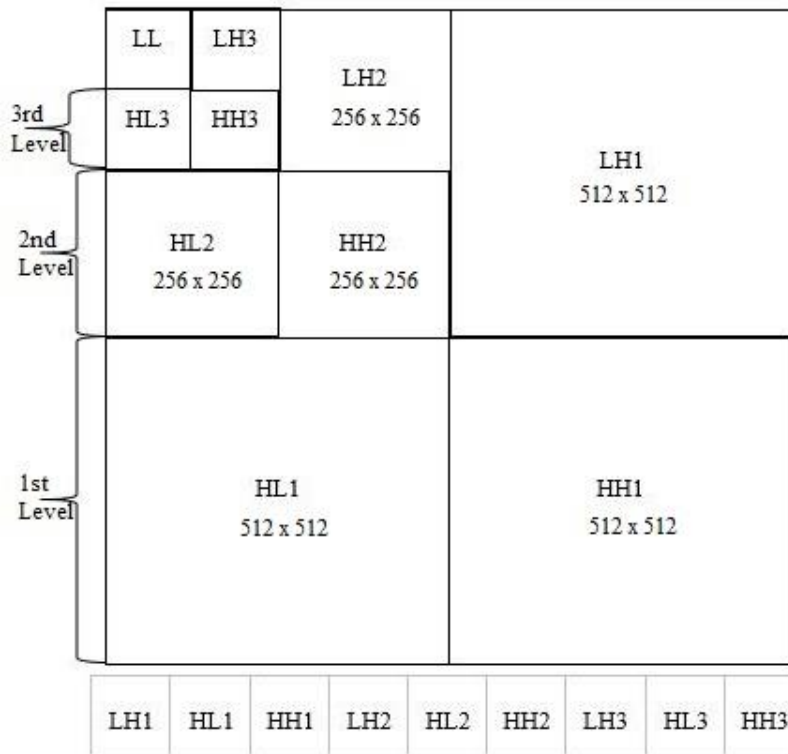
Fig.4. 9. Level decomposition in 2D- Discrete Wavelet Transform.
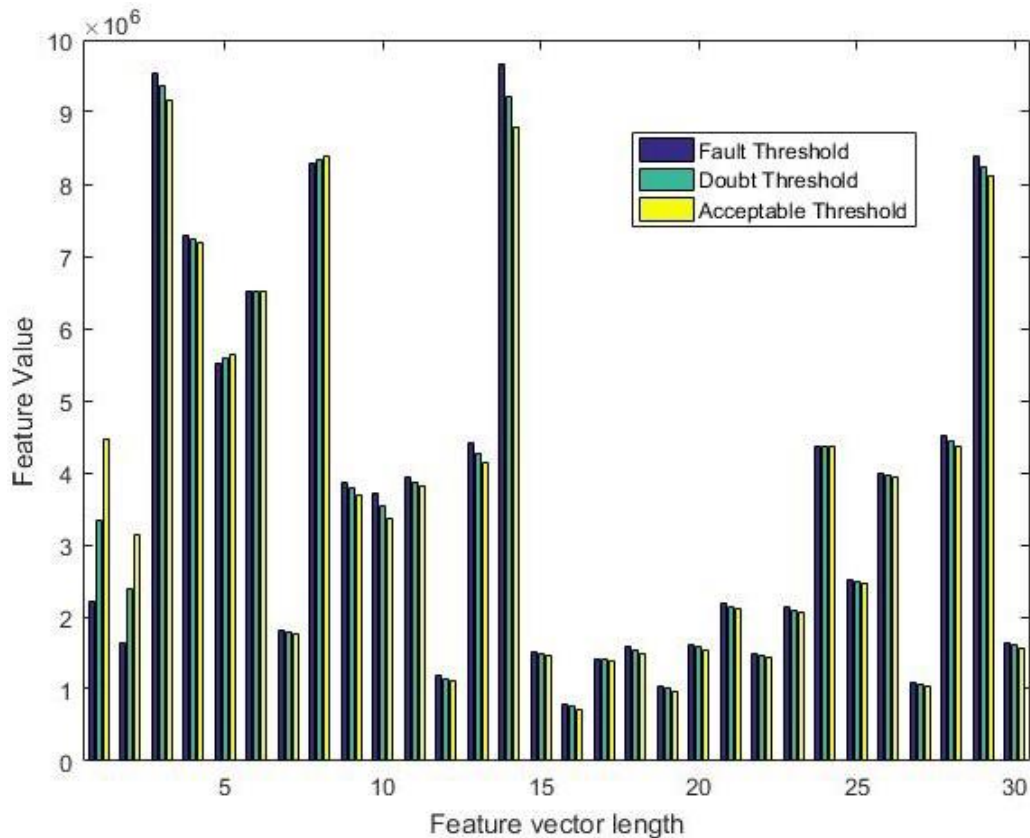
Fig. 4.10. Threshold comparison between different bins across all elements in a feature vector.

In the first case, little can be done to avoid false detection; one possible explanation for its occurrence may be some sort of unacceptable noise in the image. False detection can be avoided in the second case if a third threshold (Doubt) is introduced in the fray, which is the mean of acceptable and faulty threshold. Fig. 4.10 displays the threshold comparison for different bins across all elements in a feature vector. If the PUT is closer to the doubt threshold than the other two, the system will not classify the PUT into either of the bins; consequently, the PUT needs further inspection for classification. Although, this is neither an accurate nor an efficient way for classification, it is a trade-off to avoid false detection.

4.3 Sample Classification

The next step in automatic optical inspection is classifying the PUT into acceptable or

fault bins. It is a critical step since there is a good chance of false classification. Although, classification can only be as good as the image acquired, setting a threshold is a very intricate task. There are various algorithms such as support vector machine (SVM), K-nearest neighbor (KNN) that can be used to achieve this [51]. Due to its simplicity and without compromising efficiency, the algorithm uses K- nearest neighbor (KNN) classifier to set the threshold and consequently classify the PUT.

4.3.1 K- Nearest Neighbor Classifier

The KNN classifier is a very powerful and reliable classifier when it comes to computer vision algorithm. In this experiment, we used four different distances to find nearest neighbors. Its functionality is based on finding the nearest neighbor to a particular vector from a given set of vectors. The KNN classifier uses three pieces of information: data, training, and group. The data contains the database image feature vector, training takes query image feature vector, and group contains various groups in which query the image is to be classified. The distance metrics we used are as follows: Euclidean distance, City block distance, cosine distance and correlation distance are evaluated using equation (8-11) respectively.

$$D_E[(u,v)] = \sqrt[2]{[(v_1 - u_1)^2 + (v_2 - u_2)^2]} \qquad (4.8)$$

$$D_{Ct}(u,v) = \sum_{i=1}^{n}|u_i - v_i| \qquad (4.9)$$

$$u.v = \|u\| \|v\| \cos\theta \qquad (4.10)$$

$$D_{Cor}(u,v) = [(d_{Cov}(u,v))/\sqrt{d_{Var}(u) * d_{Var}(v)}] \qquad (4.11)$$

where, *u= (u1, u2..., un)* is the database image feature vector, *v= (v1, v2..., vn)* is the query image feature vector, *dcov* is the distance covariance, and *dvar* is the distance standard deviation.

4.3.2 Image subtraction

In this section, we discuss a method we used to classify the phase images reconstructed using shape from polarization approach. Ideally, the phase images of a fault free part should be identical as phase images are purely based on the geometry contrast. We exploit this property of the phase image to classify the faulty and fault free part. Figure 4.11 demonstrates the algorithm used. First, we create a database of fault free phase images. The number of images in this database does not reflect on the performance efficiency of this algorithm as the phase image of any fault free part will essentially have identical information. Nonetheless, we take the phase images of five unique fault free parts for the database. Second, we take the mean of the parts in the database, as it is important to regularize the variations if any in the phase images. Finally, we find a binarized image, which highlight a fault if any by using following set of equations:

$$\mu^{u,v} = \frac{1}{N}\sum_{i=1}^{N} f_i^{u,v} \tag{4.12}$$

$$\mu_{mag} = |\mu^{u,v}| \tag{4.13}$$

$$\mu_{phase} = Arg(\mu^{u,v}) \tag{4.14}$$

$$\sigma_\mu = \sqrt[2]{-2\ln\mu_{mag}} \tag{4.15}$$

$$\overline{\emptyset} = \left|\frac{F^{u,v} - \mu^{u,v})}{\sigma_\mu}\right| \tag{4.16}$$

$$\overline{\emptyset}_{bin} = \lim_{i<0} \overline{\emptyset}_i \tag{4.17}$$

Here, $\mu^{u,v}$ is the complex mean of the fault free database phase images, μ_{mag} is the magnitude of the circular mean, μ_{phase} is the phase of the circular mean; σ_μ represents the standard deviation of the mean of the fault free database images, $\overline{\emptyset}$ is the normalized phase difference

between the PUT and circular mean of the fault free database phase images and $\overline{\emptyset}_{bin}$ is the

binarized value of the phase difference. Once a binarized image is generated, if a fault is present

by using the blob detection algorithm, we automatically can classify as well as localize the PUT.
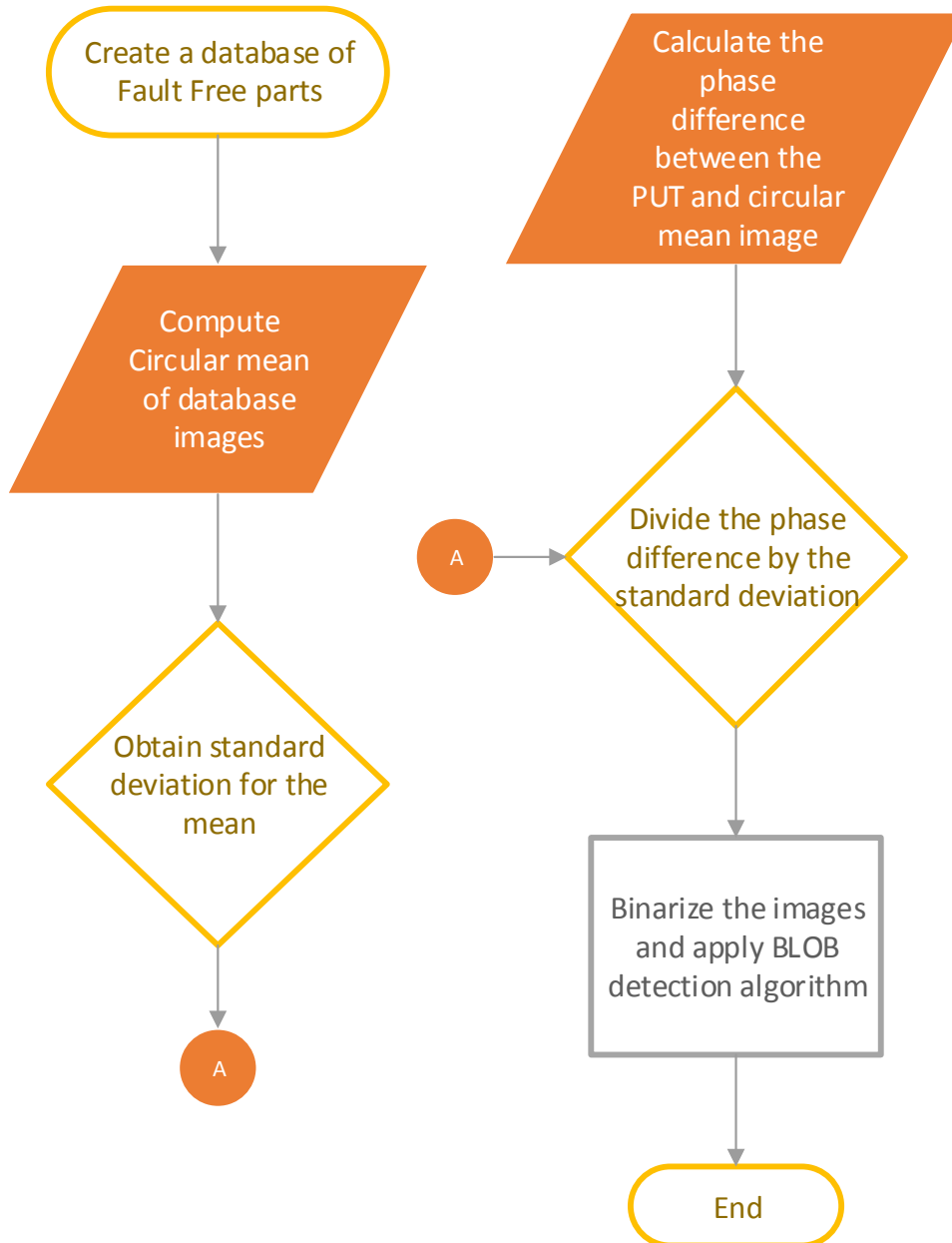
Fig. 4.11. Image subtraction algorithm used for classifying the PUT and localizing the fault (if any).

Chapter 5 Results and Discussion

The algorithm is implemented using MATLAB R2016a on a workstation with a core i7 processor having a 3.4GHz clock speed. The testing time for the PUT includes the image reading and pre-processing, feature extraction, and classification. As the images were taken manually and due to lack of consistency in the images captured in both the approaches, we developed an algorithm, which will register the image based on the reference image, using affine transforms so that all the images have minimum pixel-to-pixel error.

5.1 Transform Domain Approach

In this section, we will discuss the results of both the discrete wavelet transform and the rotated wavelet transform. Fifteen production parts were tested, of which ten were faulty parts and five were good parts. The parts are classified in three bins: good, faulty, and doubt. If the part is classified into the doubt bin, then it is considered a miss detection since the system cannot classify the part as good or faulty. The threshold associated with this bin is the arithmetic mean of good and faulty threshold as described in Chapter 4. This is done to avoid false classification. The result of this experiment is compiled in Fig. 5.1. From Fig. 5.1a, it can be said conclusively that DB5 has an accurate detection percentage in line with the Biorthogonal spline especially using the cosine and correlation classifiers. In addition, it can be observed in Fig. 5.1b that the false detection rate is least in DB5 across all distance metrics used.

Similarly, the experiment was conducted using the 2D- Rotated Wavelet Transform and the results are compiled in Fig. 5.2. It is no surprise that the DB5 outperforms the rest of the wavelets as seen in Fig. 5.1a. The Biorthogonal spline, especially using the cosine and correlation classifier, is on par with the Debauchies family. In addition, it can be observed in Fig. 5.2b that for the correlation distance metric the DB5 does not falsely classify the PUT.

Accurate Detection Comparison for Different Wavelet and Classifier Combination

(a)

False Detection Comparison for Different Wavelet and Classifier Combination

(b)

44

Miss Detection Comparison for Different Wavelet and Classifier Combination
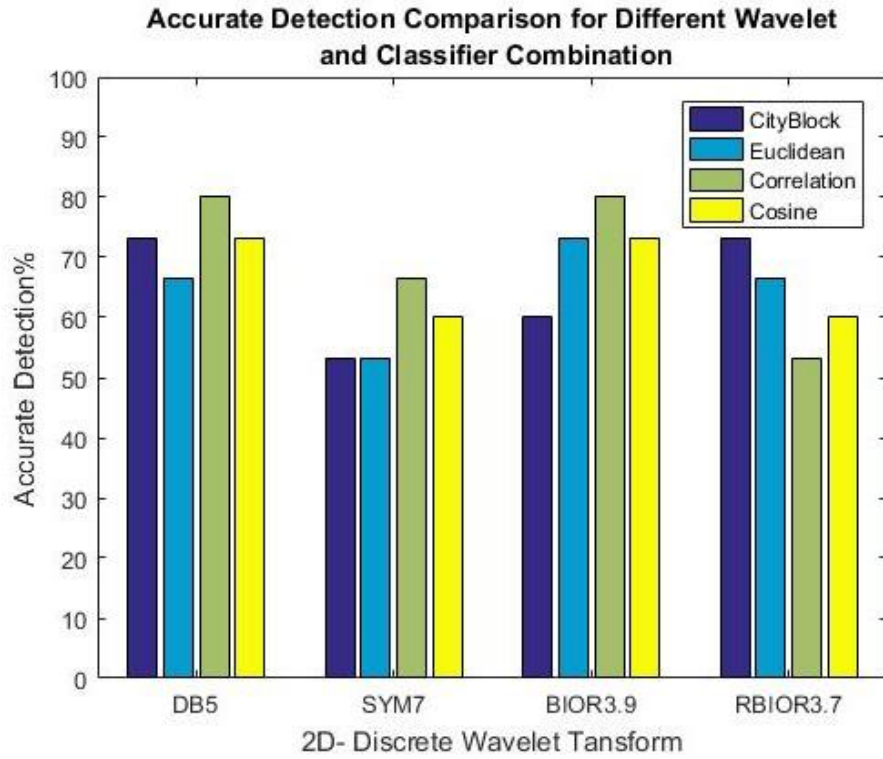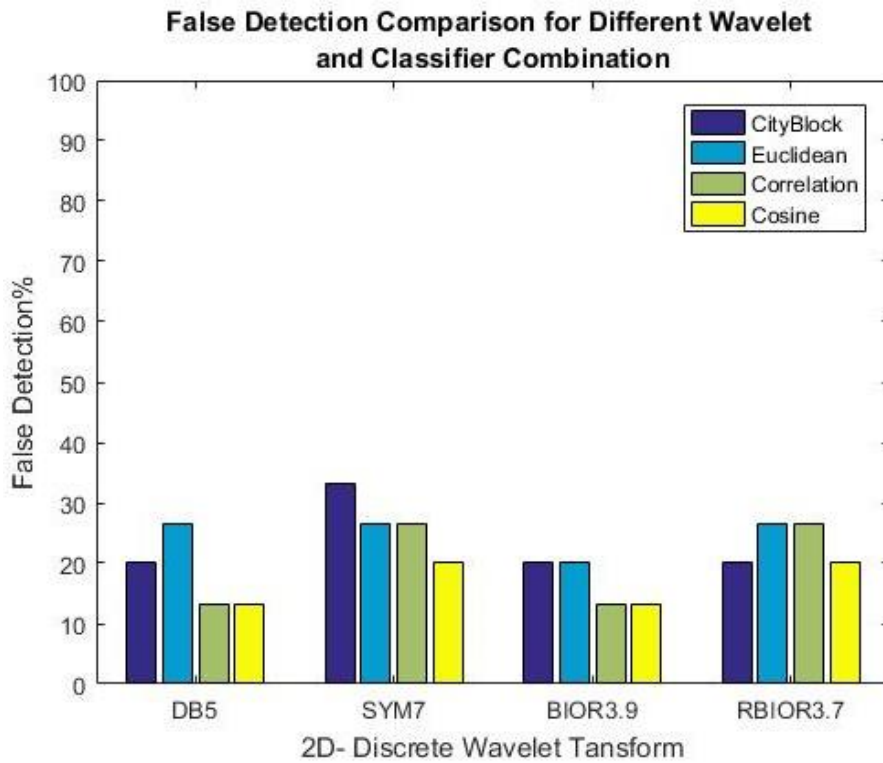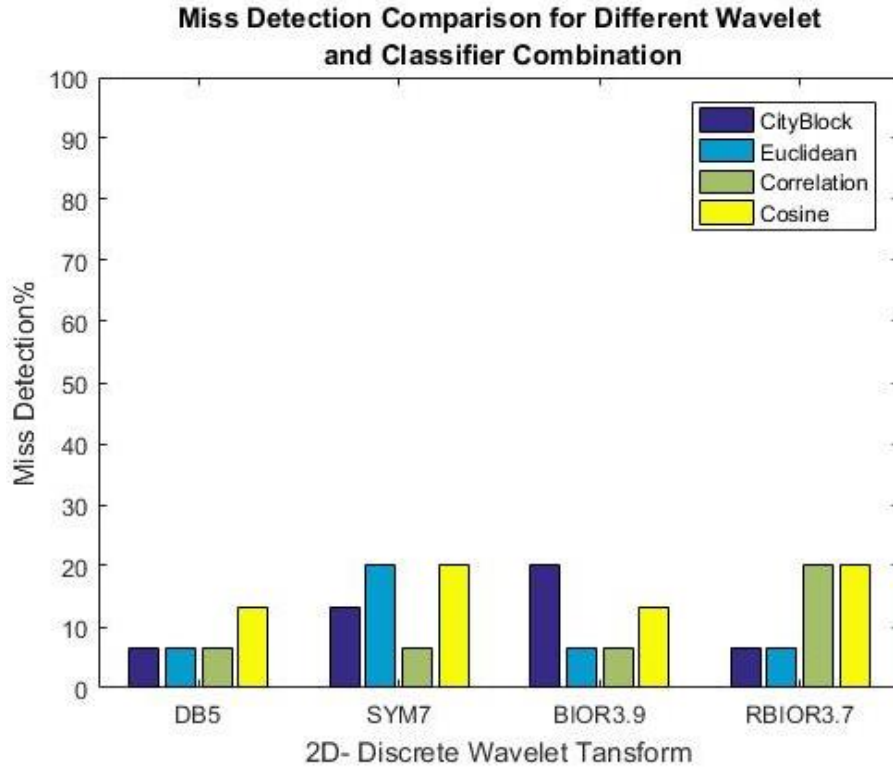
(c)

Fig. 5.1. Comparison between detection rates for different wavelet and classifier combination. (a) Accurate detection comparison. (b) False detection comparison. (c) Miss detection comparison.

The symlets in general exhibited poor efficiency along with the reverse biorthogonal splines, while the biorthogonal splines present promising efficiency across all distance metrics. Although the algorithm cannot suppress false detection completely, the idea of introducing a third threshold level to reduce false detection appears promising. A sample of a PUT that is falsely detected, and a sample of PUT which missed detection after applying the 'DB5' wavelet and using a correlation distance metric in the KNN classifier, are presented in Fig. 5.3 (a-b) and Fig 5.4, for Discrete Wavelet Transform and Rotated wavelet transform, respectively. Considering the level decomposition and classification, the computational complexity of the proposed algorithm is quite satisfactory.

(a)

(b)

Miss Detection Comparison for Different Wavelet and Classifier Combination
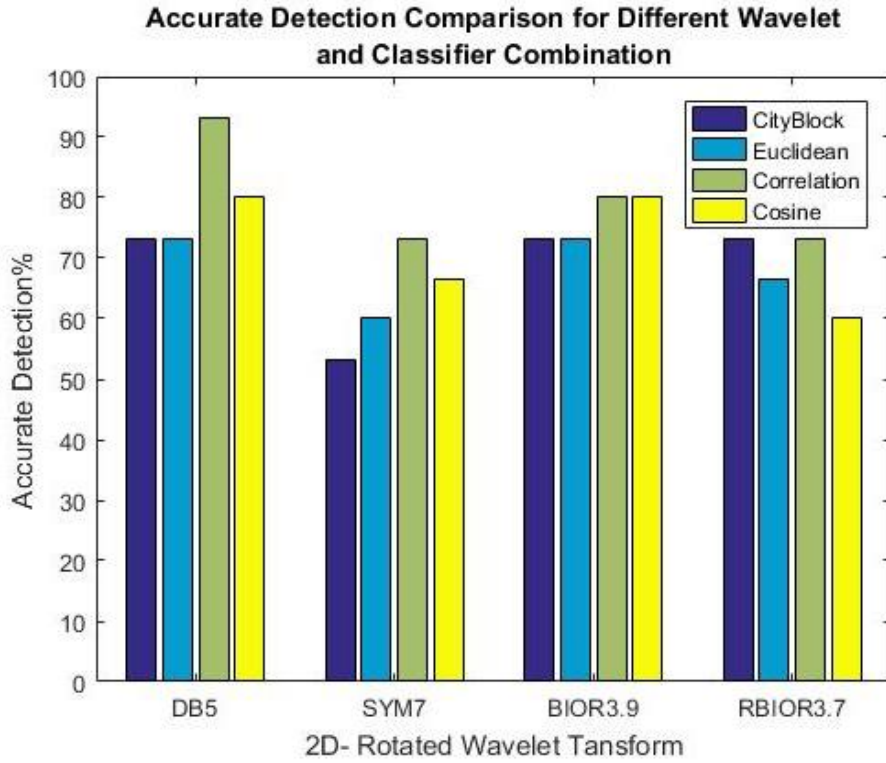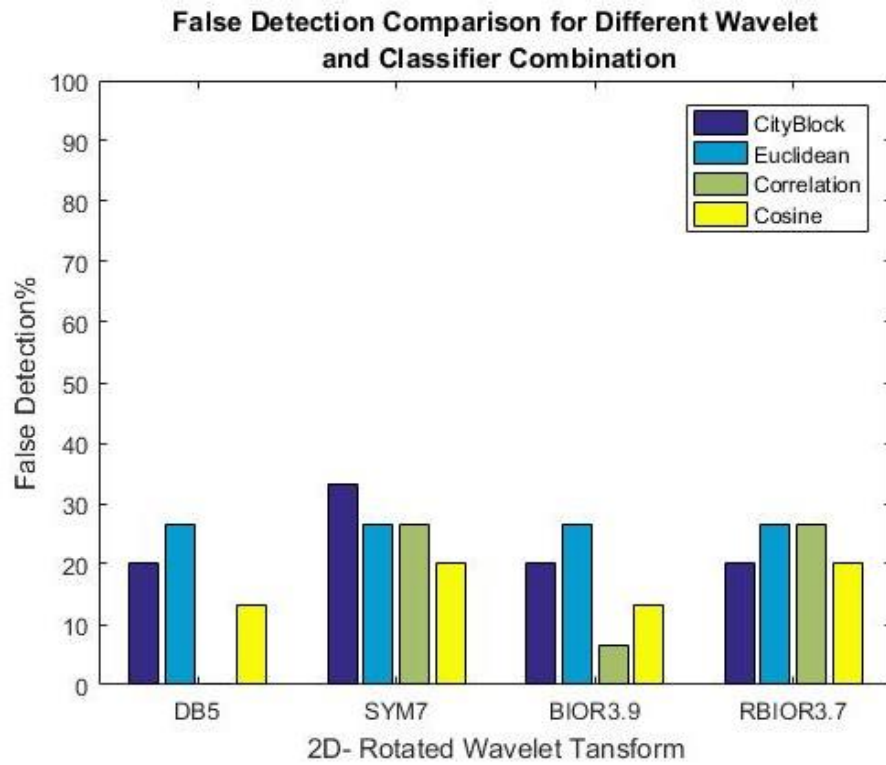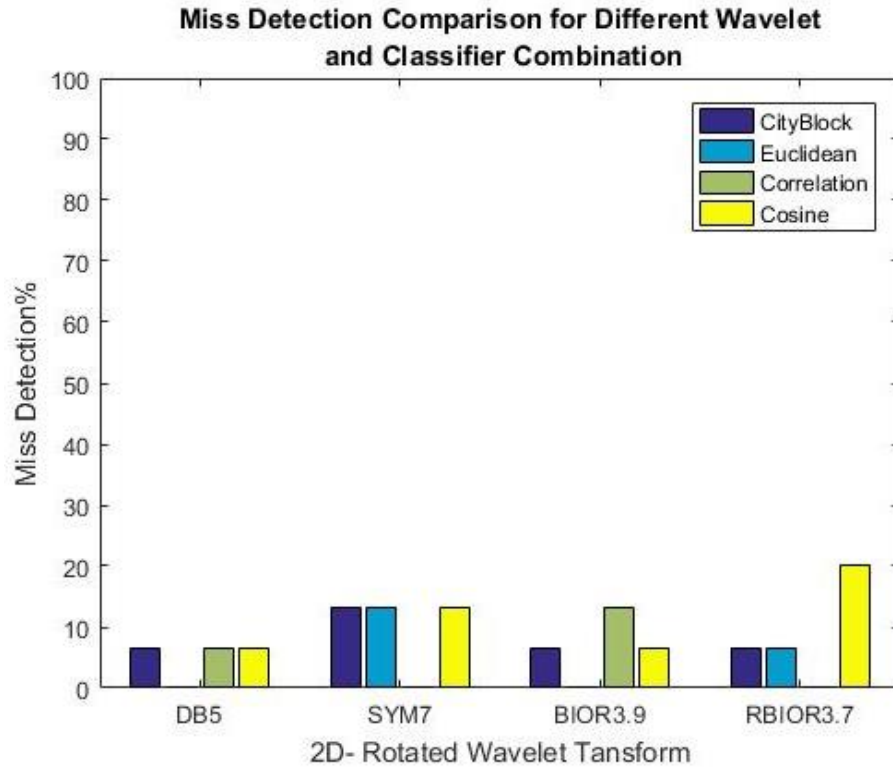
(c)

Fig. 5.2. Comparison between detection rates for different wavelet and classifier combination. (a) Accurate detection comparison. (b) False detection comparison. (c) Miss detection comparison.

Although the algorithm cannot suppress the false detection completely, the idea of introducing a third threshold level to reduce the false detection appears promising. A sample of a PUT that is falsely detected, and a sample of a PUT which missed detection after applying the 'DB5' wavelet and using a correlation distance metric in the KNN classifier, are presented in Fig. 5.3(a-b) and in Fig. 5.4 for the Discrete Wavelet Transform and the Rotated wavelet Transform, respectively. Considering the level decomposition and classification, the computational complexity of the proposed algorithm is quite satisfactory. As seen in Fig. 5.5, the testing time for DB5 is irrespective of the distance metric used for the classification.

47

False Detection of Noise as a Hole

(a)

Missed Excess Metal Fault

(b)

Fig. 5.3. (a) Sample of a PUT, which was falsely classified as a faulty part. (b) Sample of a PUT, which was not classified as faulty nor acceptable part after using 'DB5' wavelet in 2D- Discrete Wavelet Transform.

Missed Fault
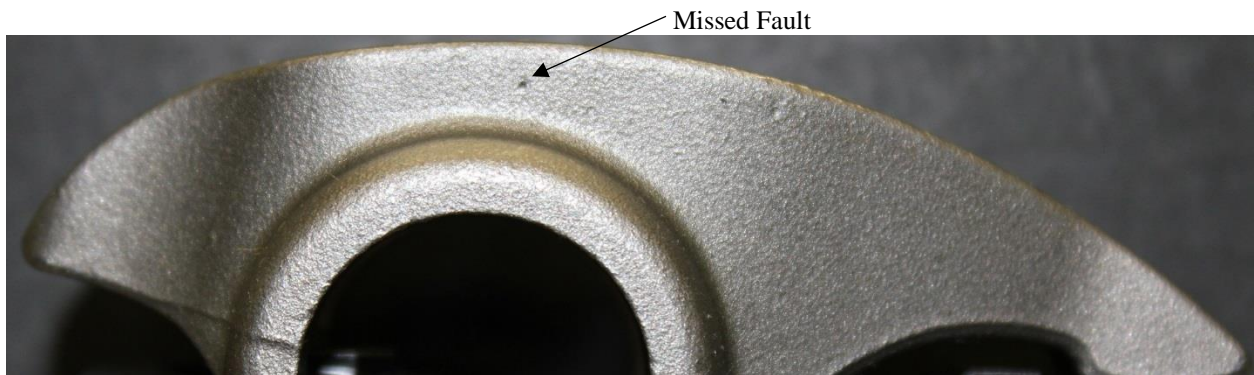
Fig. 5.4. Sample of a PUT, which was not, classified as faulty or acceptable part after using 'DB5' wavelet in 2D-Rotated Wavelet Transform.

Table I compares the classification percentage when DWT and RWT using DB5 wavelet is used for feature extraction. Clearly, an improvement in classification efficiency is seen as RWT negates some of the drawbacks of DWT. Since the algorithm uses a DB5 wavelet, the number of low pass and high pass coefficients is ten, which makes the size of RWF 19 x 19. Despite being more computationally complex than the conventional 2D-DWT, the proposed 2D-RWT is on par with 2D-DWT in terms of testing time.

TABLE I

COMPARISON BETWEEN CLASSIFICATION PERCENTAGE AND TESTING TIME FOR DB5 WAVELET ACROSS ALL DISTANCE METRICS FOR 2D-DWT AND 2D-RWT (1-LEVEL DECOMPOSITION)

Transform	Parameters	KNN Classifier Distance Metrics			
		City-Block	Euclidean	Correlation	Cosine
2D-DWT	Accurate Classification %	53.33	66.67	73.33	66.67
	False Classification %	26.67	6.67	6.67	13.33
	Miss Classification %	20	26.67	20	20
	Testing Time (in secs)	2.38	2.39	2.4	2.39
2D-RWT	Accurate Classification %	73.33	73.33	93.33	80
	False Classification %	20	26.66	0	13.33
	Miss Classification %	6.66	0	6.66	6.66
	Testing Time (in secs)	2.41	2.43	2.44	2.43
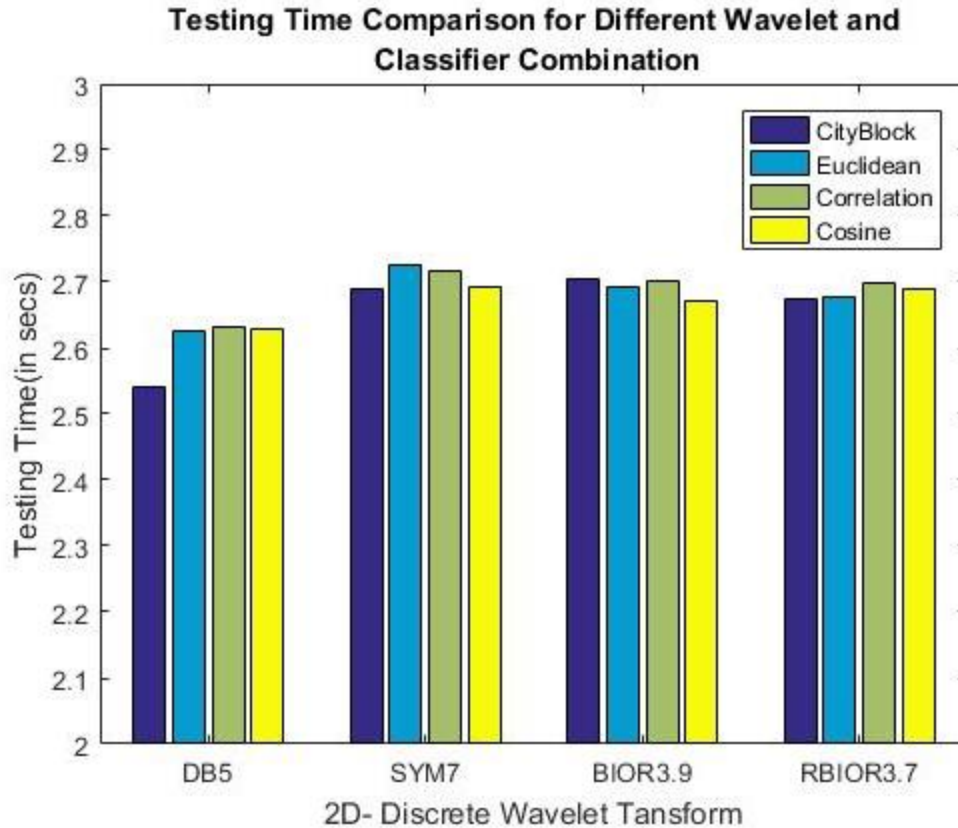
Fig. 5.5. Testing time comparison for different wavelet and classifier combination.

5.2 Shape from Polarization Approach

In this section we will discuss the results from shape from polarization approach. As described in Chapter 4, a database of phase images of fault free parts is created. Next, by using Eqn. (4.12) we can generate a mean of these phase images and use it as a template to classify the PUT. Fig. 5.6 demonstrates the phase image representation of the circular mean of the fault free database phase images. The standard deviation of this circular mean is obtained by using Eqn. (4.15) and the result is shown in Fig. 5.7. Due to some noise observed in the standard deviation, we can smooth it out using a Gaussian filter. The resultant standard deviation is displayed in Fig. 5.8. This step completes the indexing part of this approach.
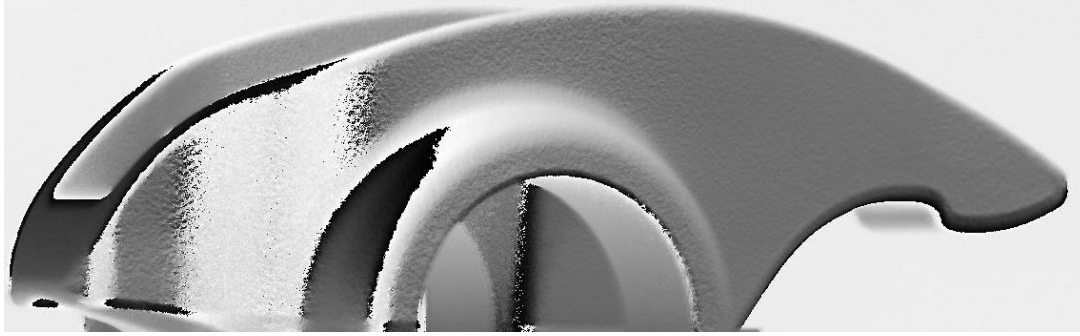
Fig 5.6. Phase image of circular mean of fault free database images.

Fig 5.7. Image representation of standard deviation of circular mean for fault free database phase images.
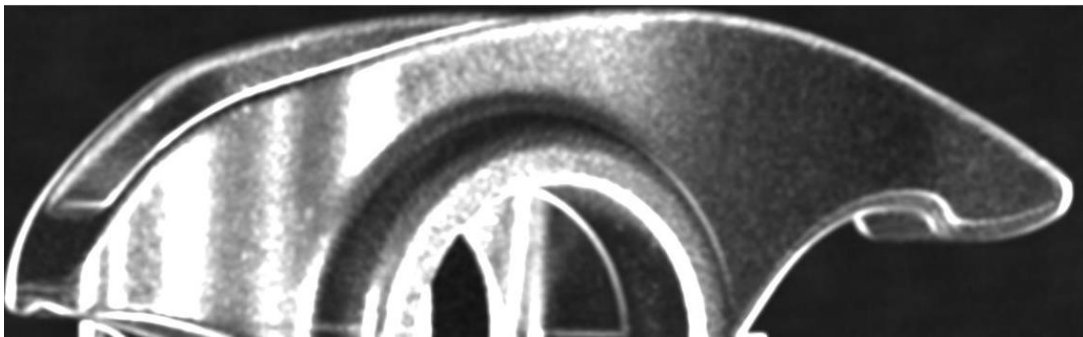
Fig 5.8. Image representation of Gaussian smoothed standard deviation of circular mean for fault free database phase images.

Regarding the testing part, the phase image of the PUT is calculated, and using Eqn. (4.16) we can calculate the normalized phase difference between the phase image of the PUT and the phase image of the Gaussian smoothed standard deviation of the circular mean for fault free database phase images. The phase image of a sample PUT and the normalized phase difference is

51

shown in Fig. 5.9 and Fig. 5.10, respectively. Once we have this phase difference using Eqn. (4.17), we binarize the image. By using the blob detection algorithm, we can classify the image into good or faulty bins. The blob detection algorithm locates the pixel position of a white space (logical 1) in the image and draws a boundary around it. By using a yes/no condition for white space detection (blob), the PUT can be classified. This method not only classifies the fault but also localizes it. Figure 5.11 show the binarized image of the phase difference image in Fig. 5.10 after implementing the blob detection algorithm. In order to validate the approach, Fig 5.12 (a-b) and Fig. 5.13 (a-b) illustrate the approach. In Figs. 5.12 and 5.13, the following distinction is made: a - phase difference image, b – binarized phase difference image after applying blob detection algorithm for faulty and fault free random samples, respectively.
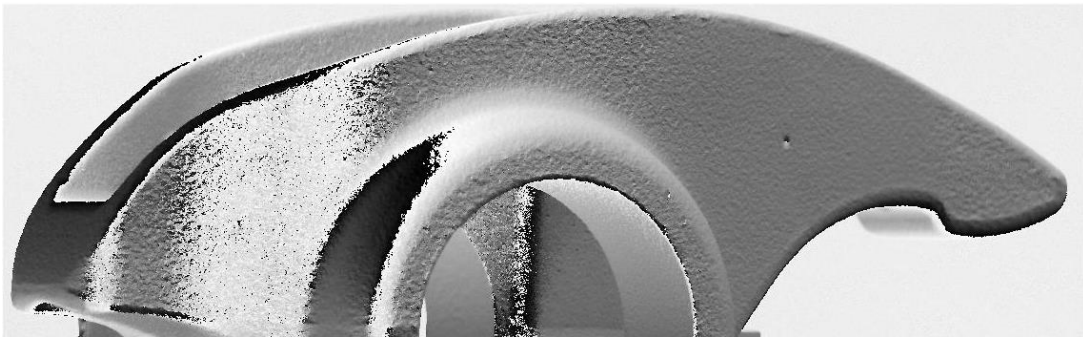
Fig 5.9. Phase image of a random sample that is under test.
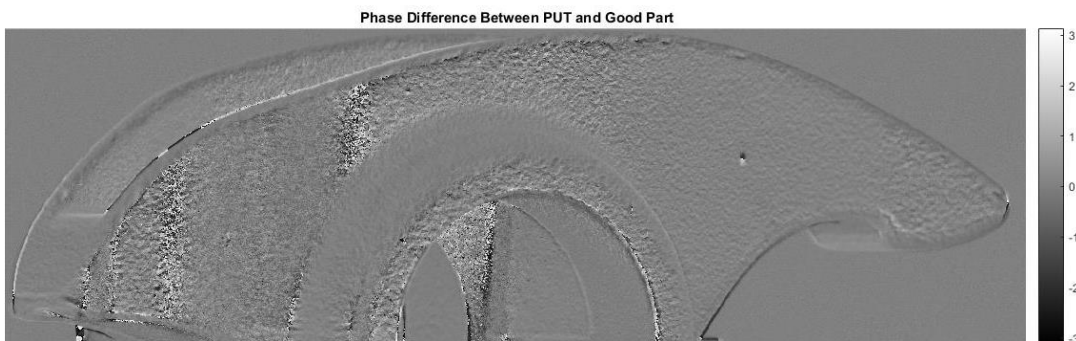
Fig 5.10. Image representation of phase difference between PUT and Gaussian smoothed standard deviation of circular mean for fault free database phase images.
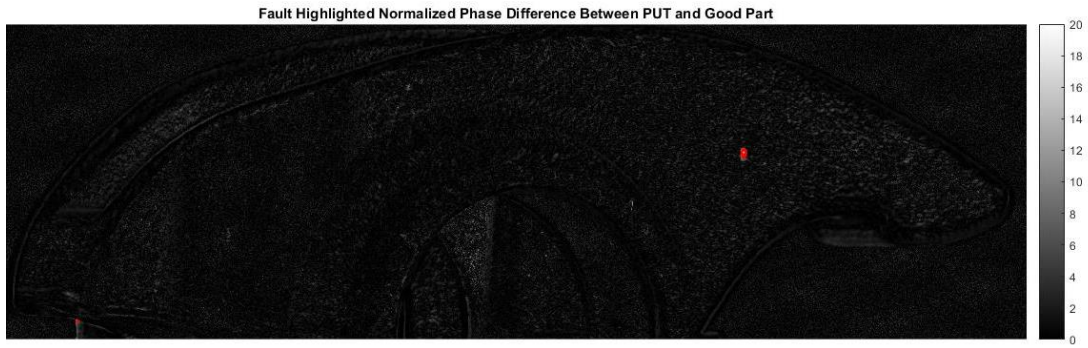
Fig 5.11.Fault highlighted by blob detection algorithm in the binarized phase difference image of a random PUT.
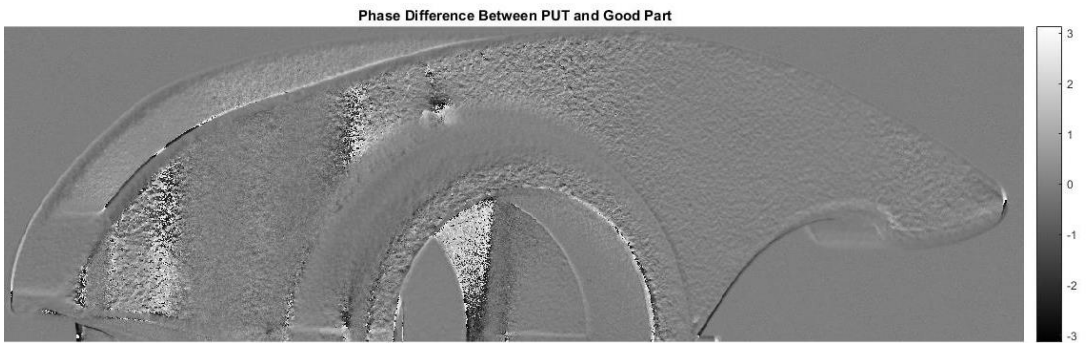
(a)
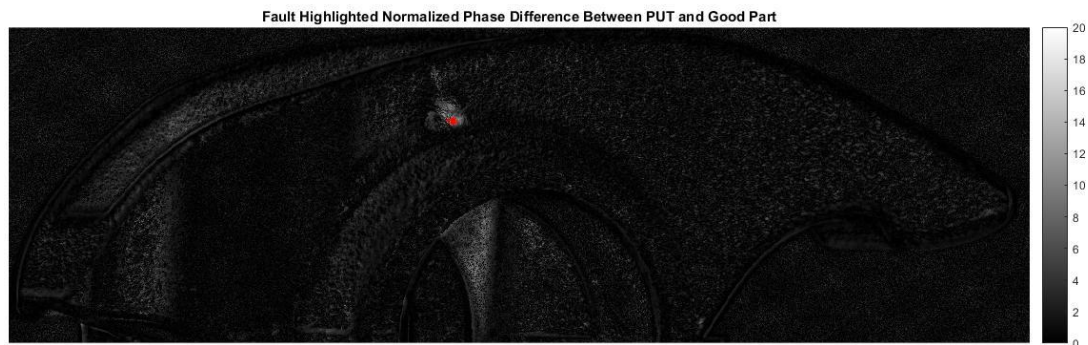
(b)

Fig 5.12.Random sample of faulty PUT. (a) Phase difference image between PUT and Gaussian smoothed standard deviation of circular mean for fault free database phase images; (b) Fault highlighted by blob detection algorithm in the binarized phase difference image of a random PUT.
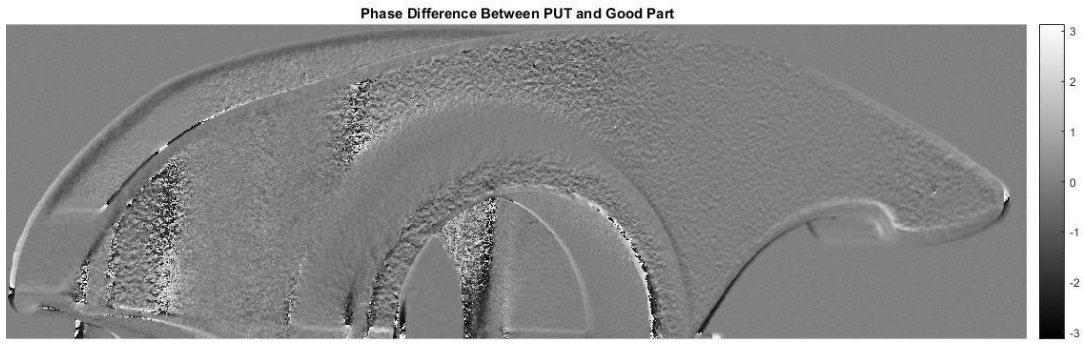
(a)

(b)

Fig 5.13. Random sample of fault free PUT. (a) Phase difference image between PUT and Gaussian smoothed standard deviation of circular mean for fault free database phase images; (b) No fault highlighted by blob detection algorithm in the binarized phase difference image of a random PUT.

Chapter 6 Conclusion

This thesis presents an optical non-destructive surface inspection algorithm for automatic classification of optical components. The inspection is carried out using customized image processing techniques. The thesis proposes a 2-D Discrete Wavelet Transform for feature extraction and a K-Nearest Neighbor Classifier for classification. A dataset of 100 images of 100 different specimens with 50 images of each bin, both acceptable and faulty, was created for indexing the threshold levels for the respective bins. These threshold levels are used to classify the PUT with the help of various distance metrics. It was observed that both Debauchies and Biorthogonal splines yielded better classification efficiency than the other discrete wavelets used in the experiment. In particular, the Debauchies 5 (DB5) wavelet and the Biorthogonal 3.9 (Bior 3.9) gave the best efficiency irrespective of the employed distance metrics. However, it is also important to consider the computational complexity when it comes to machine vision applications.

A major risk associated with most computer vision applications is false detection and it was observed in this application as well. False detection might be a result of drawbacks related to the discrete wavelet transform, or the quality of the images used for indexing as well as testing. Importantly, the algorithm maintains a good balance between computational complexity and classification efficiency. Our research demonstrates the effect of emissivity of the metallic surface on the efficiency of the system despite of the overcoming the drawbacks associated with the Discrete Wavelet Transform.

This thesis proposes a new image acquisition technique in the form of shape from polarization to negate the effect of emissivity. In this scheme, we attach a polarizer in front of a

camera lens to exploit the partially linearly polarization of the reflected light from the PUT. Eight images per part were captured by rotating the polarizer in steps of 45º. A phase image was reconstructed using these images, which depend only on geometric contrast of the part. As the phase image does not depend on the illumination, the emissivity of the part does not play any role. In order to automatically classify the PUT, a database of phase images of fault free parts is created. Further, the complex mean of these images is taken, which will serve as a template to classify a faulty part from a fault free part. The simplest way to classify the part is to subtract the phase image from the template. Then the phase difference is normalized by dividing it with a Gaussian smoothed standard deviation of the template. The resulting image is then binarized. This is a critical step, as any distortions will be automatically highlighted. Further, a blob detection algorithm is implemented to highlight the boundaries of the fault (if any).

Finally, if a comparison has to be made in between these two approaches, the transform domain approach (DWT, RWT) can achieve the accurate classification efficiency of 90%, while we expect the shape from polarization to achieve 100% classification efficiency in a best-case scenario. The shape from polarization approach not only classifies the PUT but also locates the fault by highlighting it. This gives it a distinct advantage over the transform domain technique. Although, the shape from polarization requires twice as much time as a transform domain approach, it is the trade off one has to bear for the promising fault classification and localization it exhibits. On the other hand, in the worst-case scenario, the performance of the shape from polarization is unknown and will be done in the future.

Future research needs to include a significant increase in the sample set in order to develop an industrially viable solution which ultimately involves the testing of tens or hundreds of thousands of parts. The current database of 100 parts cannot provide sufficient robustness.

Furthermore, because of the large volume testing requirements efforts have to focus on reducing the evaluation times, either by developing faster software modules or by exploring novel computer architectures that can be implemented via FPGA systems (see Appendix B). Perhaps most critical is the part handling process which needs to be mechanically robust in order to ensure the same part-by-part orientation. This may be accomplished with the aid of a manipulator or a robotic arm.

References

[1]   J. Song, S. Kim, Z. Liu, N. N. Quang and F. Bien, "A Real Time Nondestructive Crack Detection System for the Automotive Stamping Process," in IEEE Transactions on Instrumentation and Measurement, vol. 65, no. 11, pp. 2434-2441, Nov. 2016.

[2]   N. Athi, S. R. Wylie, J. D. Cullen, A. I. Al-Shamma'a, T. Sun, "Ultrasonic non-destructive evaluation for spot welding in the automotive industry", Proc. IEEE Sensors, pp. 1518-1523, Oct. 2009.

[3]   M. N. Bassim, M. P. Dudar, R. Rifaat, R. Roller, "Application of acoustic emission for nondestructive evaluation of utility inductive reactors", IEEE Trans. Power Del., vol. 8, no. 1, pp. 281-284, Jan. 1993.

[4]   H. N. Nagamani, T. B. Shanker, V. Vaidhyanathan, S. Neelakantan, "Acoustic emission technique for detection and location of simulated defects in power transformers", Proc. IEEE Russia Power Tech, pp. 1-7, Jun. 2005.

[5]   J. J. G. de la Rosa, R. Piotrkowski, J. E. Ruzzante, "Higher order statistics and independent component analysis for spectral characterization of acoustic emission signals in steel pipes", IEEE Trans. Instrum. Meas., vol. 56, no. 6, pp. 2312-2321, Dec. 2007.

[6]   J. Lim, T. Kaewkongka, "Micro cracking in stainless steel pipe detection by using acoustic emission and crest factor technique", Proc. IEEE Instrum. Meas. Technol. Conf. (IMTC), pp. 1-3, May 2007.

[7]   E. Coffey, "Acoustic resonance testing," 2012 Future of Instrumentation International Workshop (FIIW) Proceedings, Gatlinburg, TN, 2012, pp. 1-2.

[8]   V. Sankaran, "Low Cost Inline NDT System for Internal Defect Detection in Automotive Components Using Acoustic Resonance Testing," Proceedings of the National Seminar & Exhibition on Non-Destructive Evaluation, NDE 2011, December 8-10, 2011.

[9]   M. Cabrera, X. Castell and R. Montoliu, "Crack detection system based on spectral analysis of an ultrasonic resonance signals," Acoustics, Speech, and Signal Processing, 2003. Proceedings. (ICASSP '03). 2003 IEEE International Conference on, 2003, pp. II-605-8 vol.2.

[10] L. Zhiyong, Z. Qinlan and L. Xiang, "New Magnetic Particle Cassette NDT Intelligent Detection Device," 2013 Fourth International Conference on Intelligent Systems Design and

Engineering   Applications,   Zhangjiajie,   2013,   pp.   403-406. doi: 10.1109/ISDEA.2013.496

[11] J. A. Buck, P. R. Underhill, J. E. Morelli and T. W. Krause, "Simultaneous Multiparameter Measurement in Pulsed Eddy Current Steam Generator Data Using Artificial Neural Networks," in IEEE Transactions on Instrumentation and Measurement, vol. 65, no. 3, pp. 672-679, March 2016.

[12] L. S. Rosado, F. M. Janeiro, P. M. Ramos, M. Piedade, "Defect characterization with eddy current testing using nonlinear-regression feature extraction and artificial neural networks", IEEE Trans. Instrum. Meas., vol. 62, no. 5, pp. 1207-1214, May 2013.

[13] A. Bernieri, L. Ferrigno, M. Laracca, M. Molinara, "Crack shape reconstruction in eddy current testing using machine learning systems for regression", IEEE Trans. Instrum. Meas., vol. 57, no. 9, pp. 1958-1968, Sep. 2008.

[14] J. A. Buck et al., "Pulsed eddy current inspection of support structures in steam generators", IEEE Sensors J., vol. 15, no. 8, pp. 4305-4312, Aug. 2015.

[15] P. Horan, P. R. Underhill, T. W. Krause, "Pulsed eddy current detection of cracks in F/A-18 inner wing spar without wing skin removal using modified principal component analysis", NDT E Int., vol. 55, no. 1, pp. 21-27, Apr. 2013.

[16] C. A. Stott, P. R. Underhill, V. K. Babbar, T. W. Krause, "Pulsed eddy current detection of cracks in multilayer aluminum lap joints", IEEE Sensors J., vol. 15, no. 2, pp. 956-962, Feb. 2015.

[17] A. Sophian, G. Y. Tian, D. Taylor, J. Rudlin, "A feature extraction technique based on principal component analysis for pulsed eddy current NDT", NDT E Int., vol. 36, no. 1, pp. 37-41, 2003.

[18] D. R. Desjardins, G. Vallières, P. P. Whalen, T. W. Krause, "Advances in transient (pulsed) eddy current for inspection of multi-layer aluminum structures in the presence of ferrous fasteners", Proc. AIP Conf., vol. 1430, no. 1, pp. 400-407, 2012.

[19] D. Vasić, V. Bilas, D. Ambruš, "Pulsed eddy-current nondestructive testing of ferromagnetic tubes", IEEE Trans. Instrum. Meas., vol. 53, no. 4, pp. 1289-1294, Aug. 2004.

[20] N. H. Jo, H.-B. Lee, "A novel feature extraction for eddy current testing of steam generator tubes", NDT E Int., vol. 42, no. 7, pp. 658-663, 2009.

[21] Y. Cheng, L. Bai, F. Yang, Y. Chen, S. Jiang and C. Yin, "Stainless Steel Weld Defect Detection Using Pulsed Inductive Thermography," in IEEE Transactions on Applied Superconductivity, vol. 26, no. 7, pp. 1-4, Oct. 2016.

[22] E. Wu, Y. Ke and B. Du, "Noncontact Laser Inspection Based on a PSD for the Inner Surface of Minidiameter Pipes," in IEEE Transactions on Instrumentation and Measurement, vol. 58, no. 7, pp. 2169-2173, July 2009.

[23] O. Dura, "Pipe inspection using a laser-based transducer and automated analysis techniques", IEEE/ASME Trans. Mechatron., vol. 8, no. 3, pp. 401-409, Sep. 2003.

[24] O. Duran, K. Althoefer and L. D. Seneviratne, "Experiments using a laser-based transducer and automated analysis techniques for pipe inspection," 2003 IEEE International Conference on Robotics and Automation (Cat. No.03CH37422), 2003, pp. 2561-2566 vol.2.

[25] Tsubouchi, T. Takaki, S. Kawaguchi, Y and Yuta, S., "A straight pipe observation from the inside by laser spot array and a TV camera," Proc. of IEEE Int. Conf. on Intelligent Robots and Systems (IROS), pp. 82-87, 2000.

[26] R. G. Dragan, I. C. Rosca, S. A. Keo and F. Breaban, "Active thermography method using an CO2 laser for thermal excitation, applied to defect detection in bioceramic materials," 2013 E-Health and Bioengineering Conference (EHB), Iasi, 2013, pp. 1-4.

[27] Huiyi Zhang and J. Jackman, "A feasibility study of wind turbine blade surface crack detection using an optical inspection method," 2013 International Conference on Renewable Energy Research and Applications (ICRERA), Madrid, 2013, pp. 847-852.

[28] Mumtaz, M., "A new approach to aircraft surface inspection based on directional energies of texture." Pattern Recognition, Aug. 2010, pp. 4404-4407

[29] Quan Shi, Ning Xi and Yifan Chen, "Development of an automatic optical measurement system for automotive part surface inspection," Proceedings, 2005 IEEE/ASME International Conference on Advanced Intelligent Mechatronics., Monterey, CA, 2005, pp. 1557-1562.

[30] F. M. Megahed, J. A. Camelio, "Real-time fault detection in manufacturing environments using face recognition techniques", Journal of Intelligent manufacturing, vol. 23, no. 3, pp. 393-408, June 2012.

[31] M. Bicego, U. Castellani and V. Murino, "Using hidden Markov models and wavelets for face recognition," 12th International Conference on Image Analysis and Processing Proceedings, 2003, pp. 52-56.

[32] L. Chun-Lin, A Tutorial of the Wavelet Transform., Department of Electrical Engineering, National Taiwan University, Taipei, Taiwan:, 2010.

[33] T. Chang and C. C. J. Kuo, "Texture analysis and classification with tree-structured wavelet transform," in *IEEE Transactions on Image Processing*, vol. 2, no. 4, pp. 429-441, Oct 1993.

[34] M. Meade, S. C. Sivakumar and W. J. Phillips, "Comparative performance of principal component analysis, gabor wavelets and discrete wavelet transforms for face recognition," in *Canadian Journal of Electrical and Computer Engineering*, vol. 30, no. 2, pp. 93-102, spring 2005.

[35] M. Vetterli, J. Kovacevic, Wavelet and Subband Coding, NJ, Englewood Cliffs:Prentice-Hall, 1995.

[36] S. Mallat, "A theory for multiresolution signal decomposition: The wavelet representation", IEEE Trans. Pattern Anal. Mach. Intell., vol. 11, pp. 674-693, Jul. 1989.

[37] R. C. Gonzalez and R. E. Woods, Eds., Digital Image Processing, Prentice Hall, 2007.

[38] E. Rank, A. Al-Khayat, T. V. Pham, Z. Saffer and M. Stark, "Comparison between DFT-, FCT-, Wavelet-, and Lattice Filter-Based Noise Reduction for ASR," *2010 IEEE RIVF International Conference on Computing & Communication Technologies, Research, Innovation, and Vision for the Future (RIVF)*, Hanoi, 2010, pp. 1-4.

[39] R. M. Borwankar, et al., "Comparative evaluation of age classification from facial images," Advances in Computing, Communications and Informatics (ICACCI), 2015 International Conference on, Kochi, 2015, pp. 2244-2249.

[40] N. G. Kingsbury, "Image Processing with Complex Wavelet", Phil. Trans. Royal Society London A, Vol. 357, Sept 1999, pp.2543-2560.

[41] N. D. Kim, S. Udpa, "Texture classification using rotated wavelet filters", *IEEE Trans. Syst. Man Cybern. A Syst. Humans*, vol. 30, no. 6, pp. 847-852, Nov. 2000.

[42] M. Kokare, P. K. Biswas and B. N. Chatterji, "Texture image retrieval using new rotated complex wavelet filters," in *IEEE Transactions on Systems, Man, and Cybernetics, Part B (Cybernetics)*, vol. 35, no. 6, pp. 1168-1178, Dec. 2005.

[43] A. B. Gonde, R. P. Maheshwari, and R. Balasubramanian, "Rotated complex wavelet transform with vocabulary tree for content based image retrieval," in Proceedings of the First International Conference on Intelligent Interactive Technologies and Multimedia, ser. IITJVI '10. New York, NY, USA: ACM, 2010, pp. 284-291. [Online]. Available: http://doi.acm.org/10.1 145/1963564. 1963614

[44] Murty, M. Narasimha and Devi, V. Susheela, "Nearest Neighbour Based Classifiers," in *Pattern Recognition: An Algorithmic Approach, 1st* ed., London, UK, Springer, 2011, pp. 48–85.

[45] Z. Voulgaris and G. D. Magoulas, "Extensions of the k Nearest Neighbour methods for classification problems," Proceedings of the 26th International conference on artificial Intelligence and Applications, 2008, pp. 23-28.

[46] B. j. Zou and M. P. Umugwaneza, "Shape-Based Trademark Retrieval Using Cosine Distance Method," *2008 Eighth International Conference on Intelligent Systems Design and Applications*, Kaohsiung, 2008, pp. 498-504.

[47] I. B. Yildiz, H. Jaeger, S. J. Kiebel, "Re-visiting the echo state property", *Neural Netw.*, vol. 35, no. 21, pp. 1-9, Nov. 2012.

[48] Morel et al, J OPT A PURE APPL OP, 45 (17), 2006, pp.4062-4068.

[49] M. Born and E. Wolf, Principles of Optics, 7th ed. (Cambridge U. Press, 1999).

[50] Z. R. Frankot, and R. Chellappa, "A method for enforcing integrability in shape from shading algorithms," IEEE Trans. Pattern Anal. Mach. Intell. 10, 439–451 (1988).

[51] W. Yin, W. Zhang and X. Sun, "A SVM- Based Multiple Faults Classification Scheme Design in Flight Control FDI System," *Second International Conference on Innovative Computing, Informatio and Control (ICICIC 2007)*, Kumamoto, 2007, pp. 187-187.

[52] S. S. Bhairannawar, R. Kumar, V. Mirji and P. S. Sindhu, "FPGA implementation of face recognition system using efficient 5/3 2D-lifting scheme," 2016 International Conference on VLSI Systems, Architectures, Technology and Applications (VLSI-SATA), Bangalore, 2016, pp. 1-5.

[53] P. Vijay and S. Gopalakrishnan, "A novel approach for and efficient implementation of 2 Level 2D DWT using ASIC and FPGA," 2013 1st International Conference on Emerging Trends and Applications in Computer Science, Shillong, 2013, pp. 242-247.

[54] Po-Cheng Wu and Liang-Gee Chen, "An efficient architecture for two-dimensional discrete wavelet transform," in IEEE Transactions on Circuits and Systems for Video Technology, vol. 11, no. 4, pp. 536-545, Apr 2001.

[55] B. Das and S. Banerjee, "A low complexity architecture for complex discrete wavelet transform," Acoustics, Speech, and Signal Processing, 2003. Proceedings. (ICASSP '03). 2003 IEEE International Conference on, 2003, pp. II-309-12 vol.2.

Appendix A

MATLAB Scripts for 2D-Discrete Wavelet Transform 2D-Rotated Wavelet Transform, Image Registration, and BLOB Detection

```
%%%%%%%%%%%%%%%%%%%%%%%%%%%%%%%%%%%%%%%%%%
% Developer   : Raunak M. Borwankar
% Description : This function performs 2-DWT using circular convolution
%%%%%%%%%%%%%%%%%%%%%%%%%%%%%%%%%%%%%%%%%%
function [LL ,LH ,HL ,HH]=wt2(a1,w)

[m ,n]=size(a1);                    % Input signal
[ld ,hd ,lr ,hr]=wfilters(w);       % Filter bank

% First Stage of DWT
z   =zeros(1,m-length(ld));
ld1=[ld z];
hd1=[hd z];
% 1-D Dwt applied on columns
for x=1:m
    temp=a1(x,:);
    temp1=cconv(temp,ld1,m);        % Circular convolution
    out(x,:)=temp1;
    temp2=a1(x,:);
    temp3=cconv(temp2,ld1,m);
    out_a(x,:)=temp3;
    temp4=a1(x,:);
    temp5=cconv(temp4,hd1,m);
    out_b(x,:)=temp5;
    temp6=a1(x,:);
    temp7=cconv(temp6,hd1,m);
    out_c(x,:)=temp7;
end
% First Stage of DWT results
% Down-sampling y 2
out1=dyaddown(out,'c');
out1a=dyaddown(out_a,'c');
out1b=dyaddown(out_b,'c');
out1c=dyaddown(out_c,'c');
```

```matlab
% Take transpose for row operation
out2=out1';
out2a=out1a';
out2b=out1b';
out2c=out1c';

% Second stage of DWT
z1=zeros(1,m-length(ld));          % size of the signal is halved
ld2=[ld z1];
hd2=[hd z1];
% 1-D Dwt applied on rows
for x=1:m/2
    temp8=out2(x,:);
    temp9=cconv(temp8,ld2,m/2);
    out3(x,:)=temp9;
    temp10=out2a(x,:);
    temp11=cconv(temp10,hd2,m/2);
    out3a(x,:)=temp11;
    temp12=out2b(x,:);
    temp13=cconv(temp12,ld2,m/2);
    out3b(x,:)=temp13;
    temp14=out2c(x,:);
    temp15=cconv(temp14,hd2,m/2);
    out3c(x,:)=temp15;
end
% Down-sampling by 2
out4=dyaddown(out3,'c');
out4a=dyaddown(out3a,'c');
out4b=dyaddown(out3b,'c');
out4c=dyaddown(out3c,'c');
% Results
LL=out4';                    % Approxiamtion Detail coefficients
LH=out4a';                   % Horizontal Detail Coefficients
HL=out4b';                   % Vertical Detail Coefficients
HH=out4c';                   % Diagonal Detail Coefficients
```

```matlab
%%%%%%%%%%%%%%%%%%%%%%%%%%%%%%%%%%%%%%%%%%%
% Developer   : Raunak M. Borwankar
% Description : This function performs 2-RWT
%%%%%%%%%%%%%%%%%%%%%%%%%%%%%%%%%%%%%%%%%%%
function [LL LH HL HH]=rotated(A,w)
 [m,n]= size(A);              % Input signal
 [F1,F2] = wfilters(w,'d');
 [m1,n1]=size(F1);
 [m2,n2]=size(F2);

 for i = 1:n1
    for j = 1:n1
       f1(i,j) = F1(i)*F1(j);
       f2(i,j) = F1(i)*F2(j);
       f3(i,j) = F2(i)*F1(j);
       f4(i,j) = F2(i)*F2(j);
    end
 end
%% Rotating Filter Matrix and Generating Results
 N1 =imrotate(f1,-45);         % Rotate by 45 degrees
 N2 =imrotate(f2,-45);
 N3 =imrotate(f3,-45);
 N4 =imrotate(f4,-45);

 for i = 1:size(N1,1)
    for j = 1:size(N1,1)
       if N1(i,j) == 0
          N1(i,j) = 0.15;
          N2(i,j) = 0.15;
          N3(i,j) = 0.15;
          N4(i,j) = 0.15;
       end
       end
 end
```

```matlab
%%%%%%%%%%%%%%%%%%%%%%%%%%%%%%%%%%%%%%%%%%%%%%%
% Developer   : Raunak M. Borwankar
% Description : This script performs image registration w.r.t. reference image
%%%%%%%%%%%%%%%%%%%%%%%%%%%%%%%%%%%%%%%%%%%%%%%

rootDir    =    'C:\Users\rmborwankar\Desktop\Raunak\Database    new\Shape    from
Polarization\SfP_0.1\Data\Results\'; % Root Dir
RefImgDir = fullfile(rootDir,['\1c' 'phase.png']);                    % Reference Image
NewImgDir = fullfile(rootDir,['\3c' 'phase.png']);                    % New image

ReferenceImage = imread(RefImgDir);
NewImage = imread(NewImgDir);

 % if images are captured from same camera; else 'multimodal'
[optimizer,metric] = imregconfig('monomodal');

% to register the images by translation, scaling and rotation
registeredImage1 = imregister(NewImage,ReferenceImage,'affine',optimizer,metric);
```

```matlab
%%%%%%%%%%%%%%%%%%%%%%%%%%%%%%%%%%%%%%%%%%
% Developer   : Raunak M. Borwankar
% Description : This script performs the Blob Detection to classify the PUT
%%%%%%%%%%%%%%%%%%%%%%%%%%%%%%%%%%%%%%%%%%

% Load cosine and sine components of complex mean for database images
load  GoodPartmean_cos;
load   GoodPartmean_sin;
% Generate phase image from the complex mean
GoodPart_mag2 = GoodPartmean_sin.^2 + GoodPartmean_cos.^2;
% Generate standard deviation of that complex mean
GoodPart_stdev = sqrt(-1*log(GoodPart_mag2));
GoodPart_Phase = atan2(GoodPartmean_sin(600:1300,175:2450),…
GoodPartmean_cos(600:1300,175:2450));
% Smoothing out the standard deviation by applying gauss filter
Noisefree_GoodPart_stdev = imgaussfilt(GoodPart_stdev(600:1300,175:2450),5);
% PUT phase image reconstruction
PUTPhase = atan2(registeredSinImage2(600:1300,175:2450,2),
registeredCosImage2(600:1300,175:2450,2));
PUTphase_diff = mod(PUTPhase - GoodPart_Phase + pi, 2*pi) - pi;

% Normalize the phase difference
PUTscore = PUTphase_diff ./Noisefree_GoodPart_stdev ;

bin_img = abs(PUTscore) > 12; % Binarize the image

% BLOB Detection
[B,L,N,A] = bwboundaries(bin_img);
for k=1:length(B),
   if(~sum(A(k,:)))
      boundary = B{k};
      plot(boundary(:,2), boundary(:,1), 'r','LineWidth',2);
      Quailty = {'Fault Free'};
else
      Quailty = {'Faulty'};
 end
end
```

Appendix B

FPGA Implementation of Rotated Wavelet Transform

This system is designed according to the rotated wavelet filter (RWF) set depicted in Chapter 2 section 2.3. It should be pointed out that the system is not exclusive to any particular wavelet family such as the Debauchies family. The algorithm was devised in such a manner as to be reconfigurable with filter coefficients of any family without affecting the throughput. Obviously, if higher order filter coefficients are used, the hardware cost will increase; however, this increase is only in terms of registers required to store the filter coefficients it does not affect the number of multipliers or adders used.

Figure B.1 shows the functional blocks of the proposed system. Owing to the similar structure, the two dimensional RWT is performed in a single block. In order to obtain all four sub-bands at the same time, the system is implemented in pipeline fashion exploiting a certain degree of parallelism. The parallelism is necessary so that both high pass and low pass stages can be implemented simultaneously with minimum tradeoff in terms of hardware resources. The system uses four adders and four multipliers to implement the entire 2D-RWT. As mentioned earlier, the system is reconfigurable and can implement the 2D-RWT with a filter bank of any size by using only four adders and multipliers. This in turn maintains the throughput of the system irrespective of the wavelet family. The edge data accumulated provides features along the orientations described in chapter 2 section 2.3 and is used for classification. This RWT algorithm ensures that the latency of each level remains the same.
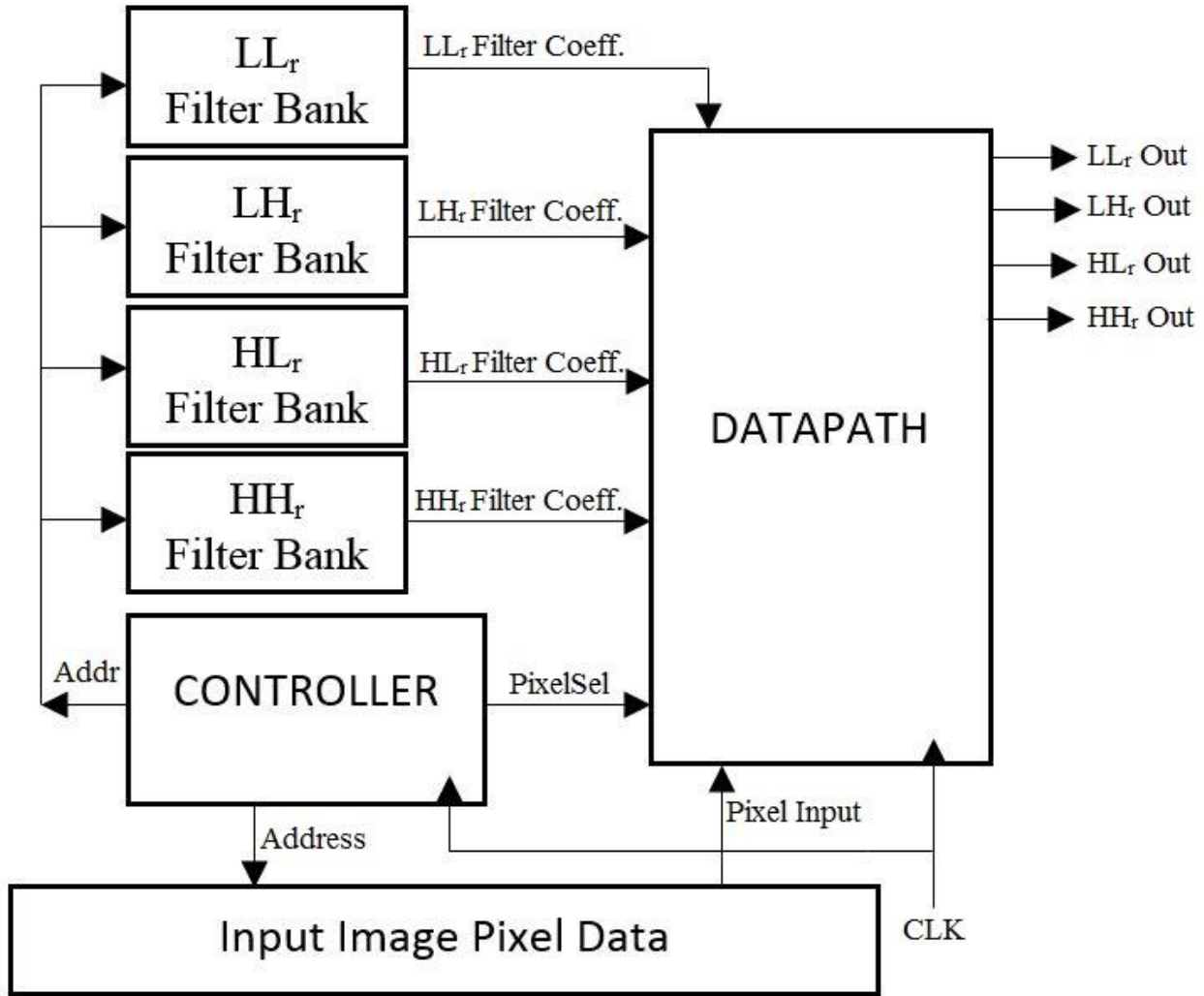
Fig. B.1. Functional block representation of the proposed 2D- RWT implementation
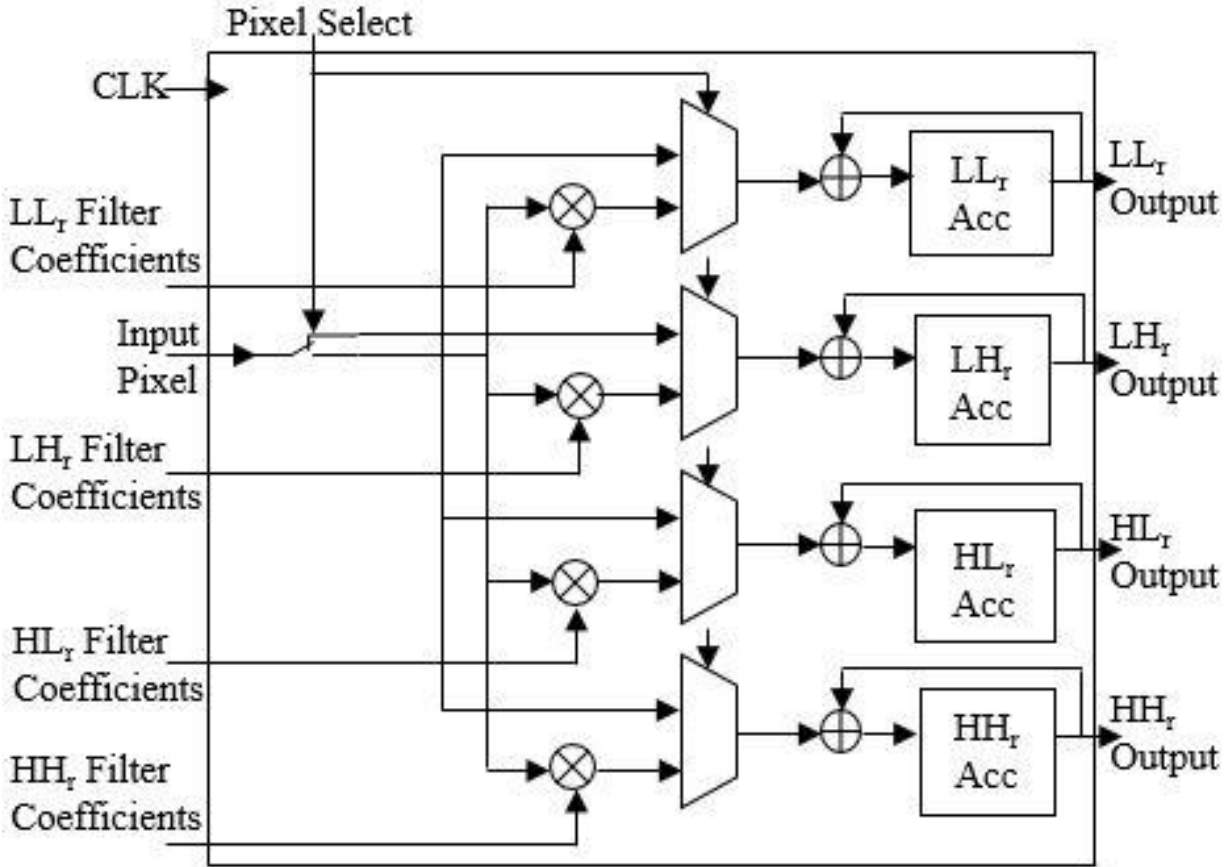
Fig. B.2. Data path representation of the proposed 2D- RWT.

Despite being more computationally complex than the conventional 2D-DWT, the proposed 2D-RWT implementation requires similar or less hardware resources. It is worth mentioning that the comparison excludes the block is memory and the resources used in the classifier. The hardware utilization, operating frequency, and dynamic power constraint are compared in Table II with some of the existing 2D-DWT architectures. Although the use of shifters instead of multipliers proposed in [54] reduces the dynamic power consumption, it adversely affects the operating frequency. The proposed RWT architecture has an operating frequency 1.5 times that of [54]. Table III shows the comparison between the number of adders and multipliers used along with the computation time in terms of clock cycles. Our work uses only four adders and the multipliers irrespective of the size of filter, which is unlike some of the

71

existing techniques. The number of clock cycles required to compute the 2D-RWT is N*M, where the input image is of size N x M. This is comparable with the existing architectures.

TABLE II

HARDWARE UTILIZATION, OPERATING FREQUENCY, AND DYNAMIC POWER COMPARISON OF PROPOSED 2D-RWT WITH EXISTING 2D-DWT METHODS

Parameter	[52]	[53] 2-level DWT	Proposed 2D-RWT
No. of Slice LUTs	1011	1974	**461**
No. of Slice Registers	302	815	**55**
Operating Frequency in MHz	207.009	141.05	**208.33**
Power in Watt	NA	**0.113**	0.150

TABLE III

COMPARISON BETWEEN NUMBER OF MULTIPLIERS, ADDERS, AND COMPUTING TIME REQUIRED IN EXISTING 2D-DWT ARCHITECTURES AND PROPOSED 2D-RWT ARCHITECTURE

Parameter	[54]	[55]	Proposed 2D-RWT
No. of Multipliers	4n	4n	**4**
No. of Adders	4n	4n	**4**
Computing Time (clock cycles)	**0.67(N*M)**	N*M	N*M

Note: N and M are the number of pixels in row and column respectively of an input image; n is size of filter.